

## Dynamo instabilities in plasmas with inhomogeneous chiral chemical potential

Jennifer Schober<sup>1,\*</sup>, Igor Rogachevskii<sup>2,3</sup> and Axel Brandenburg<sup>3,4,5,6</sup>

<sup>1</sup>*Laboratoire d'Astrophysique, EPFL, CH-1290 Sauverny, Switzerland*

<sup>2</sup>*Department of Mechanical Engineering, Ben-Gurion University of the Negev, P.O. Box 653, Beer-Sheva 84105, Israel*

<sup>3</sup>*Nordita, KTH Royal Institute of Technology and Stockholm University, 10691 Stockholm, Sweden*

<sup>4</sup>*The Oskar Klein Centre, Department of Astronomy, Stockholm University, AlbaNova, SE-10691 Stockholm, Sweden*

<sup>5</sup>*School of Natural Sciences and Medicine, Ilia State University, 0194 Tbilisi, Georgia*

<sup>6</sup>*McWilliams Center for Cosmology and Department of Physics, Carnegie Mellon University, Pittsburgh, Pennsylvania 15213, USA*

 (Received 27 July 2021; accepted 22 December 2021; published 9 February 2022)

We study the dynamics of magnetic fields in chiral magnetohydrodynamics, which takes into account the effects of an additional electric current related to the chiral magnetic effect in high-energy plasmas. We perform direct numerical simulations, considering weak seed magnetic fields and inhomogeneities of the chiral chemical potential  $\mu_5$  with a zero mean. We demonstrate that a small-scale chiral dynamo can occur in such plasmas if fluctuations of  $\mu_5$  are correlated on length scales that are much larger than the scale on which the dynamo growth rate reaches its maximum. Magnetic fluctuations grow by many orders of magnitude due to the small-scale chiral dynamo instability. Once the nonlinear backreaction of the generated magnetic field on fluctuations of  $\mu_5$  sets in, the ratio of these scales decreases and the dynamo saturates. When magnetic fluctuations grow sufficiently to drive turbulence via the Lorentz force before reaching maximum field strength, an additional mean-field dynamo phase is identified. The mean magnetic field grows on a scale that is larger than the integral scale of turbulence after the amplification of the fluctuating component saturates. The growth rate of the mean magnetic field is caused by a magnetic  $\alpha$  effect that is proportional to the current helicity. With the onset of turbulence, the power spectrum of  $\mu_5$  develops a universal  $k^{-1}$  scaling independently of its initial shape, while the magnetic energy spectrum approaches a  $k^{-3}$  scaling.

DOI: [10.1103/PhysRevD.105.043507](https://doi.org/10.1103/PhysRevD.105.043507)

### I. INTRODUCTION

The macroscopic dynamics of magnetized plasmas can be described by an effective one-fluid model, namely magnetohydrodynamics (MHD). The set of variables in MHD includes the fluid density  $\rho$ , the velocity  $\mathbf{U}$ , and the magnetic field  $\mathbf{B}$ , which are evolved by the continuity equation, the Navier-Stokes equation, and the induction equation, respectively. Together with an equation of state, this constitutes the basic MHD equations in a dynamical theory. One field of research within MHD is dynamo theory [1–7] which describes the amplification of an initially weak seed magnetic field by conversion of kinetic (mostly turbulent) energy into magnetic energy. Dynamo theory is used primarily in planetary physics and astrophysics, to understand the observed strength and structure of magnetic fields in planets [8–10], stars [11–13], and galaxies [14–18].

At very high energies, however, MHD necessarily needs to be extended to include the electric current caused by the chiral magnetic effect (CME) [19]. This macroscopic quantum effect describes the coupling between the chiral chemical potential  $\mu_5$ , i.e., the difference between the number density of left- and right-handed fermions, and magnetic helicity  $\mathcal{H}$ . To account for the CME in the modeling of high-energy plasma,  $\mu_5$  has to be included as an additional dynamical variable in the evolution equation describing the physics of the CME. The effective theory of a plasma with nonzero  $\mu_5$  is referred to as chiral MHD [20–23], which is an extension of classical MHD. Due to the CME, magnetic field and magnetic helicity can be amplified by many orders of magnitude by a chiral dynamo instability [21,24–26].

A central property of chiral MHD is the conservation of total chirality (the sum of mean magnetic helicity  $\langle \mathcal{H} \rangle$  and  $\langle \mu_5 \rangle$  multiplied by the inverse chiral nonlinearity parameter), whereas in MHD,  $\langle \mathcal{H} \rangle$  is conserved in the limit of

\*jennifer.schober@epfl.ch

vanishing magnetic resistivity. The conservation law in chiral MHD has important consequences: the conversion of  $\langle \mu_5 \rangle$  to  $\langle \mathcal{H} \rangle$  leads to a transfer of magnetic energy from small to large spatial scales, i.e., a chirally induced inverse cascade [27–29]. Depending on the initial condition,  $\mu_5$  can also be generated at the expense of magnetic helicity [30].

The extension from MHD to chiral MHD is required for all systems where fermions can be considered as being effectively massless, i.e., where the kinetic energy of the fermions exceed their rest energy significantly. In this case, chirality flipping reactions are suppressed [31]. The critical energy scale where this transition occurs depends on the exact value of the chirality flipping rate which is still under debate [32]. Nevertheless, typical examples of such systems are the high-energy plasma generated in heavy ion collisions [33–36], and, indeed, signatures of the CME have been observed at the Relativistic Heavy Ion Collider [37] and the Large Hadron Collider [38]. However, in view of a number of background effects, there is ambiguity in the interpretation of the experimental results [34]. Furthermore, there is also the chiral vortical effect (CVE) [34]. It may be important in the nonlinear stage of the magnetic field evolution, especially when strong chiral turbulence is produced. However, since chiral turbulence is usually magnetically dominated, the CVE is likely to be subdominant.

Chiral MHD has also been applied to high-energy astrophysical plasmas like the early Universe [24–26,39] and proto-neutron stars [40–44] where, in particular, the evolution of the magnetic field has been studied. Beyond that, chiral MHD can be used to describe the dynamics of new materials, like Weyl and Dirac semimetals [45]. Here, the chirality of the massless quasiparticles allows for the occurrence of the CME and an effective description of the system by chiral MHD.

In the framework of chiral MHD, the effects of coupling between magnetic and velocity fields were analyzed by means of a mean-field theory [21]. This way, a new turbulent  $\alpha_\mu$  effect was identified that is based on fluctuations of  $\mu_5$  and, contrary to the classical kinetic  $\alpha_K$  effect, is not sourced by kinetic helicity. The  $\alpha_\mu$  effect causes a mean-field dynamo instability resulting in the generation of a mean magnetic field at a length scale that is larger than the integral scale of turbulence. The mean-field dynamo was observed in direct numerical simulations (DNS) [26,46,47] and the existence of the  $\alpha_\mu$  effect was confirmed. The mean-field dynamo leads to an even more efficient transfer of magnetic energy to larger spatial scales.

The initial conditions of the previously mentioned studies of chiral dynamos included a mean chiral chemical potential which was extended over the entire simulation domain, e.g., there was a nonzero volume average  $\langle \mu_5 \rangle$  or a constant difference between right- and left-handed fermions. In our accompanying Letter [48], it was first shown in DNS that locally nonzero fluctuations of  $\mu_5$  can also

induce a small-scale chiral dynamo, even if the mean chiral chemical potential  $\langle \mu_5 \rangle$  is vanishing. As a consequence of this small-scale chiral dynamo instability, magnetically dominated turbulence is driven, which leads to the production of a  $\langle \mu_5 \rangle$  and ultimately generates a mean magnetic field via a large-scale turbulent dynamo. As argued above, the CVE [34] is likely to be subdominant in magnetically dominated turbulence and its detailed investigation will therefore be postponed to a subsequent study focusing specifically on this effect.

The present paper serves as a companion to Ref. [48] and focuses on a technical analysis of the properties of chiral dynamos that are sourced by an inhomogeneous initial  $\mu_5$ . To this end, we are extending the study of Ref. [48] by systematically exploring simulations with different initial inhomogeneities of  $\mu_5$ , starting with a two-dimensional toy model in Sec. III. With this model we explore the conditions under which a small-scale chiral dynamo can operate. In particular we test how the growth rate of the chiral dynamo depends on the separation of scales in the system. The value of the maximum possible growth rate of the small-scale chiral dynamo is determined. In Sec. IV, we present high-resolution simulations in which turbulence is generated in a self-consistent way, i.e., via the Lorentz force of the magnetic field produced by the small-scale chiral dynamo. We analyze the different contributions to the large-scale dynamo growth rate and the evolution of the power spectra in chiral MHD with initially vanishing  $\langle \mu_5 \rangle$ . Conclusions are drawn in Sec. V.

## II. PHYSICAL BACKGROUND AND METHODS

### A. Evolution equations of a chiral plasma

In spatial regions, where the chemical potentials of left-handed ( $\mu_L$ ) and right-handed ( $\mu_R$ ) fermions differ from one another, i.e., where the chiral chemical potential  $\mu_5 \equiv \mu_L - \mu_R$  is nonzero, an additional electric current arises due to the chiral magnetic effect. This current exists in addition to the Ohmic current and leads to an extension of the induction equation to the case of high-energy plasma and, therefore, the classical MHD equations.

In chiral MHD, the set of equations is given by

$$\frac{\partial \mathbf{B}}{\partial t} = \nabla \times [\mathbf{U} \times \mathbf{B} + \eta(\mu_5 \mathbf{B} - \nabla \times \mathbf{B})], \quad (1)$$

$$\rho \frac{D\mathbf{U}}{Dt} = (\nabla \times \mathbf{B}) \times \mathbf{B} - \nabla p + \nabla \cdot \boldsymbol{\tau}, \quad (2)$$

$$\frac{D\rho}{Dt} = -\rho \nabla \cdot \mathbf{U}, \quad (3)$$

together with the evolution equation of  $\mu_5$ :

$$\frac{D\mu_5}{Dt} = \mathcal{D}_5(\mu_5) + \lambda \eta [\mathbf{B} \cdot (\nabla \times \mathbf{B}) - \mu_5 \mathbf{B}^2] - \mu_5 \nabla \cdot \mathbf{U}. \quad (4)$$

In this set of equations, the magnetic field  $\mathbf{B}$  is normalized such that the magnetic energy density is  $\mathbf{B}^2/2$ ,  $\mathbf{U}$  is the velocity field, and  $\rho$  is the mass density. The advective derivative is written as  $D/Dt = \partial/\partial t + \mathbf{U} \cdot \nabla$ . Further,  $\eta$  is the microscopic magnetic diffusivity,  $p$  is the fluid pressure,  $\boldsymbol{\tau} = 2\nu\rho\mathbf{S}$  is the stress tensor,  $\mathbf{S}$  is the trace-free strain tensor with components  $S_{ij} = (U_{i,j} + U_{j,i})/2 - \delta_{ij}(\nabla \cdot \mathbf{U})/3$  (commas denote partial spatial derivatives), and  $\nu$  is the kinematic viscosity. In Eq. (4) for the chiral chemical potential  $\mu_5$ , a diffusion term characterized by the diffusion operator  $\mathcal{D}_5(\mu_5)$  has been introduced for numerical stability; see Sec. II F for details. Further,  $\lambda$  is the chiral nonlinearity parameter which quantifies the coupling between magnetic helicity and  $\mu_5$ . The system of Eqs. (1)–(4) implies that total chirality  $\chi_{\text{tot}} \equiv \langle \mathcal{H} \rangle + 2\langle \mu_5 \rangle/\lambda$  is conserved [33,34], where angle brackets denote volume averaging and  $\langle \mathcal{H} \rangle = \langle \mathbf{A} \cdot \mathbf{B} \rangle$  is the magnetic helicity,  $\mathbf{B} = \nabla \times \mathbf{A}$  is the magnetic field strength with the vector potential  $\mathbf{A}$ . The addition of the term  $-\mu_5 \nabla \cdot \mathbf{U}$  in Eq. (4) relative to Ref. [21] does not make a noticeable difference; see the appendix of Ref. [49]. This conservation law would need to be extended if the CVE were to be included.

In the system of Eqs. (1)–(4), we do not include the evolution equation for the chemical potential  $\mu \equiv \mu_L + \mu_R$ . The inclusion of this equation allows to describe the chiral magnetic waves [50]. The existence of the chiral magnetic waves requires the presence of a significant equilibrium magnetic field. In particular, the frequency of the chiral magnetic waves is proportional to the equilibrium magnetic field. However, since we consider a dynamo excited from a very small seed magnetic field, the chiral magnetic waves do not exist in our system unless the generated mean magnetic field reaches a high enough strength.

### B. Initial conditions

We study the generation of the magnetic field by fluctuations  $\mu_5'$  of the chiral chemical potential with a zero mean value  $\langle \mu_5 \rangle(t_0) = 0$  at the initial time  $t_0$ . Initially, velocity fluctuations vanish and there is a weak seed magnetic field  $\mathbf{B}$ .

The focus of this study lies on cases in which  $\mu_5$  is inhomogeneous, but we will also discuss the comparison to runs with an initially homogeneous  $\mu_5$ . In particular, the following different cases are considered:

- (a) Systems with an initial  $\mu_5$  in the form of a sine spatial profile along the  $x$  axis, i.e.,  $\mu_5(t_0, \mathbf{x}) = \mu_5(t_0, x) = \mu_{5,0} \sin(k_x x)$ . The wave number of the sine function  $k_x$  will be varied.
- (ii) Random distributions of  $\mu_5$  at different wave numbers that are initialized such that the spectrum of the chiral chemical potential,  $E_5$ , takes the form of a power-law function in  $k$  space, i.e.,  $E_5(t_0) \propto k^{-n}$ . The power law exponent  $n$  will be varied. Further, we will consider

cases where this initial condition includes a nonzero initial  $\langle \mu_5 \rangle$  and cases where  $\langle \mu_5 \rangle(t_0) = 0$ .

- (iii) Systems with a uniform distribution of the chiral chemical potential,  $\mu_5(t_0, \mathbf{x}) = \text{const}$ , that serve as comparison with previous results.

### C. Small-scale chiral dynamo

The initial condition (iii) with the homogeneous distribution of  $\mu_5$  has been used in previous studies and is well understood. For a spatially constant  $\mu_5$ , a plane-wave ansatz for the linearized induction equation (1) with the CME term and a vanishing velocity field yields a dynamo instability that is characterized by the growth rate [24]

$$\gamma(k) = |v_5 k| - \eta k^2, \quad (5)$$

with  $k$  being the wave number and  $v_5 \equiv \eta\mu_5$ . The maximum growth rate of this instability is

$$\gamma_5 = \frac{v_5^2}{4\eta}, \quad (6)$$

and it is attained at the wave number

$$k_5 = \frac{|\mu_5|}{2}. \quad (7)$$

The chiral dynamo instability is associated with the  $\nabla \times (v_5 \mathbf{B})$  term in the induction equation (1) of chiral MHD. We note that, while this term is formally similar to the kinetic  $\alpha$  effect,  $\alpha_K$  (that is related to the kinetic helicity), i.e., it is similar to the  $\nabla \times (\alpha_K \mathbf{B})$  term in the induction equation in the classical mean-field MHD, the effect described by the  $v_5$  term is not caused by turbulence, but rather by a quantum effect related to the handedness of fermions. By analogy with the classical dynamo caused by the  $\alpha_K$  effect, the small-scale chiral dynamo is referred to as the  $v_5$  dynamo. In the presence of shear, its growth rate is modified in ways that are similar to those of the classical  $\alpha\Omega$  dynamo [21], except that, again, this chiral dynamo is not related to a turbulent flow.

### D. Production of the mean chiral chemical potential

Fluctuations of the chiral chemical potential  $\mu_5'$  cause an exponential growth of the magnetic field by the  $v_5$  dynamo. During the  $v_5$  dynamo phase, magnetic fluctuations produce velocity fluctuations by the Lorentz force, i.e., the term  $(\nabla \times \mathbf{B}) \times \mathbf{B}$  on the right-hand side of Eq. (2).

Since the initial mean chiral chemical potential is zero, and the magnetic helicity  $\langle \mathbf{a} \cdot \mathbf{b} \rangle$  of the seed magnetic field vanishes, the total initial chirality vanishes as well,  $\chi_{\text{tot}}(t_0) = 0$ . Here  $\mathbf{a}$  and  $\mathbf{b}$  are fluctuations of the vector potential and the magnetic field. Due to the conservation of total chirality, it is zero at all times:  $\chi_{\text{tot}}(t) = 0$ . Initial

fluctuations of a chiral chemical potential  $\mu'_5$  with a wide range of scales, however, produce magnetic fluctuations  $\mathbf{b}$  by the  $v_5$  dynamo. In particular, for a wide spectrum in  $k$  space, fluctuations of the chiral chemical potential at larger scales then serve as a *mean field* for fluctuations on smaller scales, so that the chiral dynamo instability excites magnetic fluctuations at small scales, and produces small-scale magnetic helicity  $\langle \mathbf{a} \cdot \mathbf{b} \rangle$  during the dynamo action. Due to the conservation of total chirality, the production of the small-scale magnetic helicity  $\langle \mathbf{a} \cdot \mathbf{b} \rangle$  causes the buildup of the mean chiral chemical potential:

$$\langle \mu_5 \rangle = -\lambda \langle \mathbf{a} \cdot \mathbf{b} \rangle / 2. \quad (8)$$

The small-scale chiral dynamo produces magnetically driven turbulence and enhances turbulent kinetic energy. The latter increases the fluid and magnetic Reynolds numbers,  $\text{Re} \equiv U_{\text{rms}} / (\nu k_{\text{int}})$  and  $\text{Re}_M \equiv U_{\text{rms}} / (\eta k_{\text{int}})$ , where

$$k_{\text{int}}^{-1} \equiv \frac{\int_1^{k_{\text{max}}} E_M(k) k^{-1} dk}{\int_1^{k_{\text{max}}} E_M(k) dk}, \quad (9)$$

is the integral scale of magnetically driven turbulence [51]. When  $\text{Re}_M$  is large enough, the mean chiral dynamo instability is excited, which can result in the generation of the mean magnetic field.

### E. Contributions to the mean-field dynamo

The mean induction equation is given by

$$\frac{\partial \bar{\mathbf{B}}}{\partial t} = \nabla \times [\bar{\mathbf{U}} \times \bar{\mathbf{B}} + (\bar{v}_5 + \alpha) \bar{\mathbf{B}} - (\eta + \eta_T) \nabla \times \bar{\mathbf{B}}], \quad (10)$$

where  $\bar{v}_\mu = \eta \bar{\mu}_5$  and the overbars indicate averages. In comparison to Eq. (1), there are two additional contributions in Eq. (10):  $\alpha$  that increases the growth rate if it has the same sign as  $\bar{v}_5$  or if  $|\alpha| \gg |\bar{v}_5|$  and the turbulent diffusion  $\eta_T \approx U_{\text{rms}} / (3k_{\text{int}})$ .

The  $\alpha$  effect itself also has different contributions. In particular, for chiral MHD with a homogeneous  $\mu_5$ , the  $\alpha_\mu$  effect has been derived in Ref. [21] and confirmed by DNS in Ref. [26]. It is related to an interaction between fluctuations of the magnetic field  $\mathbf{b}$  and the chiral chemical potential  $\mu'_5$ . For very small mean magnetic energy (in comparison to the turbulent kinetic energy),  $\alpha_\mu$  has the form [21]

$$\alpha_\mu = -\frac{2}{3} \bar{v}_5 \ln(\text{Re}_M). \quad (11)$$

When the turbulent magnetic energy  $\bar{b}^2$  is much larger than the turbulent kinetic energy  $\bar{u}^2$  (so called magnetically driven turbulence), the magnetic  $\alpha$  effect,

$$\alpha_M = C_M \tau_c \chi_c, \quad (12)$$

plays a key role in the mean-field dynamo, where  $\chi_c = \overline{\mathbf{b} \cdot (\nabla \times \mathbf{b})}$  is the current helicity. For weakly inhomogeneous turbulence, the current helicity is estimated as  $\chi_c \approx \langle \mathbf{a} \cdot \mathbf{b} \rangle_{\text{int}} k_{\text{int}}^2$ , i.e., it is proportional to the small-scale magnetic helicity  $\overline{\mathbf{a} \cdot \mathbf{b}} \equiv \langle \mathbf{a} \cdot \mathbf{b} \rangle_{\text{int}}$  (see Ref. [52]), where  $\langle \dots \rangle_{\text{int}}$  implies averaging over the integral scale of turbulence. The correlation time of the magnetically driven turbulence is the Alfvén time  $\tau_c = (u_A k_{\text{int}})^{-1}$ , based on the integral scale given  $k_{\text{int}}^{-1}$  and the Alfvén speed  $u_A = (\bar{b}^2)^{1/2} \approx B_{\text{rms}}$ . The mean fluid density entering in the Alfvén speed  $u_A$  and  $\alpha_M$  is unity and for large magnetic Reynolds numbers the coefficient  $C_M = 2(q-1)/(q+1)$  depends on the exponent  $q$  of the magnetic energy spectrum  $k^{-q}$ . Finally, there can be a contribution of the kinetic  $\alpha$  effect that is caused by kinetic helicity:

$$\alpha_K = -\frac{1}{3} \tau_c \chi_K. \quad (13)$$

However, kinetic helicity  $\chi_K = \langle \mathbf{u} \cdot \boldsymbol{\omega} \rangle_{\text{int}}$  is not produced efficiently in magnetically driven turbulence and therefore  $\alpha_K$  is a subdominant effect in the system considered in this work. Here  $\boldsymbol{\omega}$  are vorticity fluctuations. This will be demonstrated later.

During the dynamo action, the small-scale magnetic helicity  $\overline{\mathbf{a} \cdot \mathbf{b}}$  and the current helicity  $\chi_c$  are evolving. The budget equation for  $\chi_c$  follows from the dynamic equation for the magnetic helicity  $\overline{\mathbf{a} \cdot \mathbf{b}}$ . In the presence of a nonzero mean magnetic field, this equation reads [21]

$$\frac{\partial}{\partial t} \overline{\mathbf{a} \cdot \mathbf{b}} + \text{div} \mathbf{F} = 2\bar{v}_5 \bar{b}^2 - 2\bar{\mathcal{E}} \cdot \bar{\mathbf{B}} - 2\eta \overline{(\nabla \times \mathbf{b})}, \quad (14)$$

where  $\bar{\mathcal{E}} \equiv \overline{\mathbf{u} \times \mathbf{b}} = \alpha_M \bar{\mathbf{B}} - \eta_T (\nabla \times \bar{\mathbf{B}})$  is the turbulent electromotive force and  $\mathbf{F}$  is the flux of  $\overline{\mathbf{a} \cdot \mathbf{b}}$ . Here we consider the case when the kinetic  $\alpha$  effect caused by the kinetic helicity and the  $\alpha_\mu$  effect [21,26] are much smaller than the magnetic  $\alpha$  effect. This is a typical situation for the chiral mean-field dynamo in a nonuniform  $\mu_5$  (see below). Near maximum field strength, two leading terms,  $2\bar{v}_5 \bar{b}^2 - 2\alpha_M \bar{B}^2$ , in Eq. (14) compensate each other, so that the magnetic  $\alpha$  effect reaches the value

$$\alpha_M^{\text{sat}} = \eta \bar{\mu}_5 \frac{\bar{b}^2}{\bar{B}^2}, \quad (15)$$

where we took into account that for large magnetic Reynolds numbers the last term on the right-hand side of Eq. (14) vanishes. This term describes the dissipation rate of the magnetic helicity with the dissipation time scale which is  $\text{Re}_M$  times larger than the correlation time in the integral scale of turbulence, where  $\text{Re}_M$  is the magnetic Reynolds number. We also take into account that the term

$-\eta_T(\nabla \times \bar{B})$  in the turbulent electromotive force is responsible for the dissipation of the mean magnetic field.

Overall, the growth rate of the mean magnetic field in the mean-field dynamo phase is given by

$$\gamma(k) = (\bar{v}_5 + \alpha)k - (\eta + \eta_T)k^2, \quad (16)$$

where  $\alpha$  represents the maximum of the different contributions. In the limit of large  $\text{Re}_M$ ,  $|\alpha| \gg |\bar{v}_5|$  and  $\eta_T \gg \eta$ , so that the maximum growth rate is

$$\gamma_\alpha = \frac{\alpha^2}{4\eta_T}, \quad (17)$$

and it is attained at the characteristic wave number

$$k_\alpha = \frac{\alpha}{2\eta_T}, \quad (18)$$

which is less than the minimum wave number in the system. In this study, we show that the mean  $\bar{v}_5$  effect,

where  $\bar{v}_5 = \eta\bar{\mu}_5$ , another mechanism of mean-field dynamo generation, is inefficient and that  $\alpha = \alpha_M$ .

## F. Numerical setup

We use the Pencil Code [53] to solve equations (1)–(4) in a three-dimensional periodic domain of size  $L^3 = (2\pi)^3$  with a resolution of up to  $672^3$ . This code employs a third-order accurate time-stepping method [54] and sixth-order explicit finite differences in space [55,56]. An overview of all runs presented in this paper is given in Table I. We note that runs R – 2, R – 1, and R + 1 have also been discussed in the companion Letter [48]. A list of notations is given in Table II.

The smallest wave number covered in the numerical domain is  $k_1 = 2\pi/L = 1$  which we use for the normalization of length scales. All velocities are normalized to the sound speed  $c_s = 1$  and further the mean fluid density is unity,  $\bar{\rho} = 1$ . Further, the magnetic Prandtl number is 1, i.e., the magnetic diffusivity equals the viscosity. Time is normalized by the diffusion time  $t_\eta = (\eta k_1^2)^{-1}$ .

TABLE I. Summary of all runs presented in this paper.

	Setup		Parameters			Initial conditions				Output		
	Dimension	Resolution	$\eta = \nu$	$\mu_5$ diffusion	$\lambda_5$	$\mu_{5,\text{max}}$	$\mu_{5,\text{rms}}$	$\langle \mu_5 \rangle$	$\mu_5$ structure	$\max(B_{\text{rms}})$	$\max(\langle \mu_5 \rangle)$	$\max(\text{Re}_M)$
Series H												
H1	3D	128 <sup>2</sup>	0.001	$\mathcal{D}_5 = 2.4 \times 10^{-7}$	$1 \times 10^2$	10	10	10	const	0.44	10	65
H2	3D	672 <sup>3</sup>	0.0002	$\mathcal{D}_5 = 1.8 \times 10^{-9}$	$4 \times 10^2$	42	42	42	const	0.41	42	$4.2 \times 10^2$
Series S												
S1	2D	128 <sup>2</sup>	0.001	$\mathcal{D}_5 = 2.4 \times 10^{-7}$	$1 \times 10^4$	10	7.1	$-7.2 \times 10^{-15}$	$\sin(1x)$	0.036	0.31	14
S1L	2D	128 <sup>2</sup>	0.001	$\mathcal{D}_{5,L} = 0.001$	$1 \times 10^4$	9.9	7.0	$9.1 \times 10^{-15}$	$\sin(1x)$	$1.9 \times 10^{-6}$	$4.5 \times 10^{-9}$	$9.5 \times 10^{-8}$
S1H3	2D	128 <sup>2</sup>	0.001	$\mathcal{D}_{5,H3} = 6.0 \times 10^{-11}$	$1 \times 10^4$	10	7.1	$-8.2 \times 10^{-15}$	$\sin(1x)$	0.037	0.31	14
S2	2D	128 <sup>2</sup>	0.001	$\mathcal{D}_5 = 2.4 \times 10^{-7}$	$1 \times 10^4$	10	7.1	$2.5 \times 10^{-16}$	$\sin(2x)$	0.04	0.14	6.1
S2 $\lambda$ 2	2D	128 <sup>2</sup>	0.001	$\mathcal{D}_5 = 2.4 \times 10^{-7}$	$1 \times 10^2$	10	7.1	$2.5 \times 10^{-16}$	$\sin(2x)$	0.11	0.05	24
S2 $\lambda$ 6	2D	128 <sup>2</sup>	0.001	$\mathcal{D}_5 = 2.4 \times 10^{-7}$	$1 \times 10^6$	10	7.1	$2.5 \times 10^{-16}$	$\sin(2x)$	0.0045	0.17	0.35
S2L	2D	128 <sup>2</sup>	0.001	$\mathcal{D}_{5,L} = 0.001$	$1 \times 10^4$	10	7.1	$2.5 \times 10^{-16}$	$\sin(2x)$	$1.8 \times 10^{-7}$	$1.9 \times 10^{-14}$	$1.6 \times 10^{-12}$
S2H3	2D	128 <sup>2</sup>	0.001	$\mathcal{D}_{5,H3} = 6.0 \times 10^{-11}$	$1 \times 10^4$	10	7.1	$2.5 \times 10^{-16}$	$\sin(2x)$	0.04	0.14	6.4
S3	2D	128 <sup>2</sup>	0.001	$\mathcal{D}_5 = 2.4 \times 10^{-7}$	$1 \times 10^4$	10	7.1	$-1.2 \times 10^{-14}$	$\sin(3x)$	0.029	0.039	3.6
S4	2D	128 <sup>2</sup>	0.001	$\mathcal{D}_5 = 2.4 \times 10^{-7}$	$1 \times 10^4$	9.9	7.1	$-1.3 \times 10^{-14}$	$\sin(4x)$	0.015	0.091	2.3
S5	2D	128 <sup>2</sup>	0.001	$\mathcal{D}_5 = 2.4 \times 10^{-7}$	$1 \times 10^4$	10	7.1	$-2.3 \times 10^{-16}$	$\sin(5x)$	$4.1 \times 10^{-7}$	$5.4 \times 10^{-11}$	$3.1 \times 10^{-9}$
S6	2D	128 <sup>2</sup>	0.001	$\mathcal{D}_5 = 2.4 \times 10^{-7}$	$1 \times 10^4$	9.9	7	$-1.1 \times 10^{-14}$	$\sin(6x)$	$5.7 \times 10^{-9}$	$1.1 \times 10^{-14}$	$1.4 \times 10^{-12}$
S8	2D	128 <sup>2</sup>	0.001	$\mathcal{D}_5 = 2.4 \times 10^{-7}$	$1 \times 10^4$	9.8	7	$-1.2 \times 10^{-14}$	$\sin(8x)$	$9 \times 10^{-9}$	$1.4 \times 10^{-14}$	$1.7 \times 10^{-12}$
S8L	2D	128 <sup>2</sup>	0.001	$\mathcal{D}_{5,L} = 0.001$	$1 \times 10^4$	5.8	4.2	$-1.3 \times 10^{-14}$	$\sin(8x)$	$5.9 \times 10^{-9}$	$1.3 \times 10^{-14}$	$1.9 \times 10^{-12}$
S8H3	2D	128 <sup>2</sup>	0.001	$\mathcal{D}_{5,H3} = 6.0 \times 10^{-11}$	$1 \times 10^4$	9.8	7.1	$-1.2 \times 10^{-14}$	$\sin(8x)$	$9 \times 10^{-9}$	$1.4 \times 10^{-14}$	$1.7 \times 10^{-12}$
S23D	3D	672 <sup>3</sup>	0.0002	$\mathcal{D}_5 = 1.8 \times 10^{-9}$	$4 \times 10^2$	50	35	$-7.1 \times 10^{-17}$	$\sin(2x)$	0.4	0.2	$3.3 \times 10^2$
S23D $\lambda$ 4	3D	672 <sup>3</sup>	0.0002	$1.8 \times 10^{-9}$	$4 \times 10^4$	50	35	$-1.6 \times 10^{-15}$	$\sin(2x)$	0.068	0.027	45
S23D $\lambda$ 8	3D	672 <sup>3</sup>	0.0002	$1.8 \times 10^{-9}$	$4 \times 10^8$	50	35	$-1.6 \times 10^{-15}$	$\sin(2x)$	0.0011	0.029	0.016
S23DL	3D	672 <sup>3</sup>	0.0002	$\mathcal{D}_{5,L} = 0.0002$	$4 \times 10^2$	50	35	$-7.1 \times 10^{-17}$	$\sin(2x)$	0.32	0.16	$4 \times 10^2$
S203D	3D	672 <sup>3</sup>	0.0002	$\mathcal{D}_5 = 1.8 \times 10^{-9}$	$4 \times 10^2$	50	35	$-1.6 \times 10^{-15}$	$\sin(20x)$	0.02	$2.4 \times 10^{-5}$	2.1
Series R												
R – 2m	3D	672 <sup>2</sup>	0.0002	$\mathcal{D}_5 = 1.8 \times 10^{-9}$	$4 \times 10^2$	46	15	–4.5	$E_5(k) \propto k^{-2}$	0.19	4.5	$2.1 \times 10^2$
R – 2	3D	672 <sup>3</sup>	0.0002	$\mathcal{D}_5 = 1.8 \times 10^{-9}$	$4 \times 10^2$	50	14	0	$E_5(k) \propto k^{-2}$	0.18	0.18	$2.7 \times 10^2$
R – 2CMW1	3D	672 <sup>3</sup>	0.0002	$\mathcal{D}_5 = 1.8 \times 10^{-9}$	$4 \times 10^2$	51	14	$-9.8 \times 10^{-16}$	$E_5(k) \propto k^{-2}$	0.18	0.28	$2.1 \times 10^2$
R – 2CMW2	3D	672 <sup>3</sup>	0.0002	$\mathcal{D}_5 = 1.8 \times 10^{-9}$	$4 \times 10^2$	51	14	$-9.8 \times 10^{-16}$	$E_5(k) \propto k^{-2}$	0.19	0.26	$2.2 \times 10^2$
R – 1	3D	672 <sup>2</sup>	0.0002	$\mathcal{D}_5 = 1.8 \times 10^{-9}$	$4 \times 10^2$	86	16	0	$E_5(k) \propto k^{-1}$	0.095	0.052	$1.3 \times 10^2$
R + 1	3D	672 <sup>3</sup>	0.0002	$\mathcal{D}_5 = 1.8 \times 10^{-9}$	$4 \times 10^2$	54	13	$-2.1 \times 10^{-15}$	$E_5(k) \propto k^{+1}$	0.068	0.055	16

TABLE II. Different characteristic wave numbers and averages.

Name	Definition	Description
Wave numbers:		
$k_1$	$\frac{2\pi}{L} = 1$	Minimum wave number in the domain with length $L = 2\pi$
$k_5$	$\frac{\mu_{5,\max}}{2}$	Wave number on which the small-scale chiral instability has its maximum
$k_p$	$\dots$	Wave number on which $E_M$ attains its maximum
$k_{\mu_5,\text{eff}}$	$\left(\frac{\int E_5(k)k^{-1}dk}{\int E_5(k)dk}\right)^{-1}$	Effective wave number on which $\mu_5$ is correlated
$k_{\text{int}}$	$\left(\frac{\int E_M(k)k^{-1}dk}{\int E_M(k)dk}\right)^{-1}$	Effective wave number on which $\mathbf{B}$ is correlated = integral scale of turbulence
Magnetic field:		
$B_{\text{rms}}$	$(2 \int E_M(k)dk)^{1/2}$	Rms magnetic field strength
$b$	$(2 \int_{k_5}^{k_{\max}} E_M(k)dk)^{1/2}$	Field strength of small-scale magnetic fluctuations
$\langle B \rangle_{\text{int}}$	$\left(\frac{\int E_M(k)^2 dk}{\int E_M(k)dk}\right)^{1/2}$	Magnetic field strength on the integral scale of turbulence
Growth rate of magnetic field:		
$\gamma_{\text{rms}}$	$\frac{d \ln(B_{\text{rms}})}{dt}$	Measured growth rate of $B_{\text{rms}}$
$\gamma_b$	$\frac{d \ln(b)}{dt}$	Measured growth rate of $b$
$\gamma_{\text{int}}$	$\frac{d \ln(\langle B \rangle_{\text{int}})}{dt}$	Measured growth rate of $\langle B \rangle_{\text{int}}$
$\gamma_5$	$\frac{\eta \mu_{5,\max}^2}{4}$	Theoretically predicted growth rate of the small-scale chiral dynamo
$\gamma_\alpha$	$\frac{(\max(\bar{\nu}_5, \alpha_M, \alpha_M))^2}{4(\eta + \eta_M)}$	Theoretically predicted growth rate of the mean-field dynamo
Magnetic helicity:		
$\langle \mathcal{H} \rangle$	$\frac{\int \mathcal{H}(\mathbf{x}) dV}{V}$	Volume average of the magnetic helicity
$\langle \mathcal{H} \rangle_{\text{int}}$	$\frac{\int H_M(k) E_M(k) dk}{\int E_M(k) dk}$	magnetic helicity on the integral scale of turbulence
Chiral chemical potential:		
$\mu_{5,\text{rms}}$	$(\int E_5(k)dk)^{1/2}$	Rms value of the chiral chemical potential
$\mu_{5,\max}$	$\max(\mu_5(\mathbf{x}))$	Maximum of the chiral chemical potential
$\langle \mu_5 \rangle$	$\frac{\int \mu_5(\mathbf{x}) dV}{V}$	Volume average of the chiral chemical potential
$\langle \mu_5 \rangle_{\text{int}}$	$\left(\frac{\int E_M(k) E_5(k) dk}{\int E_M(k) dk}\right)^{1/2}$	Chiral chemical potential on the integral scale of turbulence
Velocity field:		
$u$	$(2 \int_{k_5}^{k_{\max}} E_K(k)dk)^{1/2}$	Field strength of small-scale velocity fluctuations

For numerical stability, the diffusion of  $\mu_5$  is required and has been introduced by the diffusion operator in Eq. (4). In our previous work with a uniform initial  $\mu_5$ , we have always used Laplacian diffusion, i.e.,  $\mathcal{D}_5(\mu_5) = \mathcal{D}_{5,L} \Delta \mu_5$  where  $\mathcal{D}_{5,L}$  is a constant and was usually set to the same value as  $\eta$ . In the present case, this would lead to an excessive loss of  $\mu_5$  fluctuations. For this work, we focus the diffusion to the very smallest length scales such that  $\mu_5$  on intermediate scales is not affected significantly. Therefore we use second-order hyperdiffusion which is given by  $\mathcal{D}_5(\mu_5) = -\mathcal{D}_5 \nabla^4 \mu_5$ . The hyperdiffusion coefficient  $\mathcal{D}_5$  is set to a value that produces the same diffusion rate on the Nyquist wave number as the one of the magnetic field for the corresponding value of  $\eta$ . In the Appendix A, we

present the results of simulations that have been repeated with Laplacian diffusion and third-order hyperdiffusion (with the diffusion constant  $\mathcal{D}_{5,H3}$ ) for comparison.

### III. 2D DNS WITH A SPATIALLY INHOMOGENEOUS INITIAL $\mu_5$

In this section we analyze series S which includes 2D simulations with a  $\mu_5$  that is set up as a sine spatial profile of  $\mu_5$  with different wave numbers. This serves as a simple toy model for an inhomogeneous initial  $\mu_5$  and allows us to understand the main differences from previously studied simulations which were set up with a constant initial value of  $\mu_5$  throughout the numerical domain.

### A. Onset of the small-scale chiral dynamo

We first consider run S2 as a representative example. Its initial rms value is  $\mu_{5,\text{rms}} \approx 7.07$  and the maximum value of the sine function in the domain is  $\mu_{5,\text{max}} = 10$ . In Fig. 1(a) the time series of several characteristic quantities is presented. The existence of fluctuations of  $\mu_5$  causes an instability in the magnetic field  $B_{\text{rms}}$ , which increases by 7 orders of magnitude. Along with the exponential increase of magnetic energy, a mean value of  $\mu_5$  is generated, reaching a maximum of  $|\langle \mu_5 \rangle| \approx 0.1$  at the time  $t \approx 1.0$ . We have repeated run S2 with  $32^2$ ,  $64^2$ , and  $256^2$  grid cells, respectively, and found that this maximum value of  $|\langle \mu_5 \rangle|$  is independent of the resolution. Initially,  $\langle \mu_5 \rangle$  is generated with a negative sign and is roughly compensated by the positive  $\lambda \langle \mathcal{H} \rangle / 2$  during the  $v_5$  dynamo phase. Both,  $\langle \mathcal{H} \rangle$  and  $\langle \mu_5 \rangle$  flip signs at  $t \approx 1.1$ , shortly after the end of the kinematic dynamo amplification.

The measured growth rate  $\gamma$  of  $B_{\text{rms}}$ ,  $\gamma_{\text{rms}}$  is compared to the theoretically predicted maximum rate of the  $v_5$  dynamo, Eq. (6), in Fig. 1(b). Therefore we test two different values of  $\mu_5$  in Eq. (6): the rms and the maximum value. Using  $\mu_{5,\text{rms}}$  tends to underestimate the observed  $\gamma$  by approximately 50% while  $\mu_{5,\text{max}}$  predicts a slightly larger growth rate than that observed (the ratio  $\gamma / (\eta \mu_{5,\text{max}}^2 / 4)$  reaches up to  $\approx 0.75$ ). Theoretically it can be expected that the growth rate of the magnetic field is highest in the region of the numerical domain where  $\mu_5$  reaches its maximum, i.e., where the amplitude of the sine spatial profile is highest. The evolution of the observed  $B_{\text{rms}}$  should then be dominated by these local instabilities. Therefore, we would expect that  $\mu_{5,\text{max}}$  should determine  $\gamma$ .

However, it could be the case that the instability cannot develop sufficiently, especially if the spatial maximum of  $\mu_5$  is localized in a small region. This is, in particular, critical if the characteristic instability length scale of the  $v_5$  dynamo, given by Eq. (7), is larger than the region in which  $\mu_5$  is correlated. For a direct comparison between the two different scales, we introduce the correlation length of  $\mu_5$  as

$$k_{\mu_5,\text{eff}}^{-1} \equiv \frac{\int E_5(k) k^{-1} dk}{\int E_5(k) dk}, \quad (19)$$

where  $E_5(k)$  is the power spectrum of  $\mu_5$ . In the case of a sine function spatial profile,  $k_{\mu_5,\text{eff}}$  corresponds, initially, roughly to the wave number of the sine function. A chiral dynamo instability can only develop properly if  $k_{\mu_5,\text{eff}} \ll k_5$ . The evolution of different characteristic wave numbers in the simulation S2 is presented in Fig. 1(c). In the beginning, the  $k_5$  is larger than  $k_{\mu_5,\text{eff}}$  by a factor of 2.5 and the peak of the magnetic energy spectrum,  $k_p$  occurs in  $\mu_{5,\text{max}}/2$ . At later times,  $k_{\mu_5,\text{eff}}$  changes through the backreaction of the magnetic field on the  $E_5$  spectrum, ultimately becoming larger than  $\mu_{5,\text{max}}/2$  for times larger

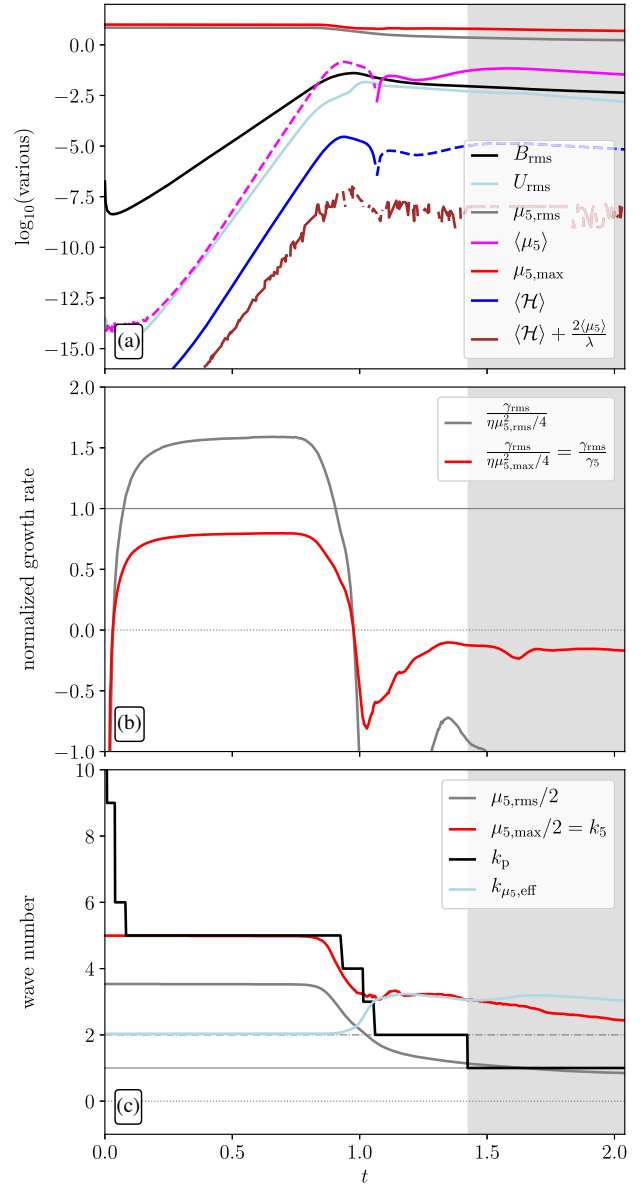


FIG. 1. Analysis for run S2: (a) Time series of the rms values of  $B$ ,  $U$ , and  $\mu_5$ . For  $\mu_5$ , the evolution of the volume average ( $\langle \mu_5 \rangle$ ) and the maximum value are also shown ( $\mu_{5,\text{max}}$ ). Finally, the volume average of magnetic helicity ( $\langle \mathcal{H} \rangle$ ) and the conserved quantity ( $\langle \mathcal{H} \rangle + 2\langle \mu_5 \rangle / \lambda$ ) are plotted. Solid line styles indicate positive sign and negative values are shown as dashed lines. (b) The measured growth rate of  $B_{\text{rms}}$  normalized by  $\eta \mu_{5,\text{rms}}^2 / 4$  (gray line) and  $\gamma_5 = \eta \mu_{5,\text{max}}^2 / 4$  (red line). (c) Different characteristic wave numbers in the simulation:  $\mu_{5,\text{rms}}/2$ ,  $k_5 = \mu_{5,\text{max}}/2$ , the wave number  $k_p$  on which  $E_M$  reaches its maximum, and the effective correlation wave number of  $\mu_5$ ,  $k_{\mu_5,\text{eff}}$ . For times larger than  $t_{k_1}$ , i.e., when the peak of the magnetic energy spectrum has reached the wave number  $k_1$ , the plots are shaded in gray.

than  $\approx 1$ . This coincides roughly with the magnetic energy maximum of the chiral dynamo.

The change of  $k_{\mu_5,\text{eff}}$  from 2 to larger values can be directly seen in the evolution of the power spectra  $E_5$  in

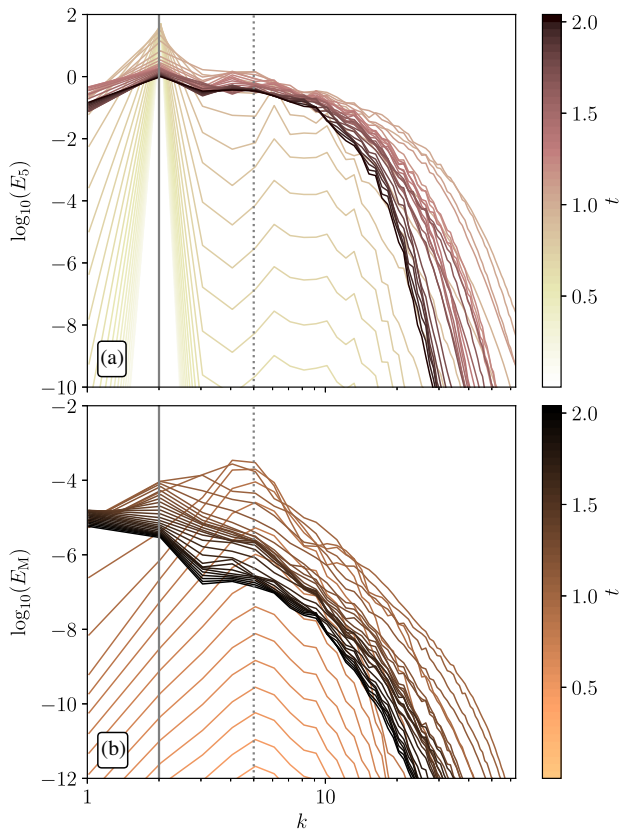


FIG. 2. Evolution of the power spectra in run S2. Lines with different colors correspond to different times as indicated by the color bars. The solid vertical line shows the position of the initial wave number of  $\mu_5$ ,  $k = 2$ , and the dotted vertical line shows the initial instability scale related to the  $v_5$  dynamo,  $\mu_{5,\max}(t_0)/2$ . (a) Power spectrum of  $\mu_5$ ,  $E_5(k, t)$ . (b) Magnetic energy spectrum  $E_M(k, t)$ .

Fig. 2(a). With the amplification of magnetic energy, shown in Fig. 2(b), the  $E_5$  spectrum also grows for wave numbers both larger and smaller than  $k = 2$ . In fact, the evolution of  $E_5$  seems to follow the one of  $E_M$ . Here, the wave number for which the instability develops most quickly is clearly  $k = 5$  which corresponds to  $k_5 = \mu_{5,\max}/2$ . This is another indication that the growth rate of the  $v_5$  dynamo is indeed given by the maximum of  $\mu_5$  in the spatial domain. However, the instability scale,  $k_5 = \mu_{5,\max}/2 = 5$  (indicated by the dotted vertical line), is close to the effective scale of  $\mu_5$ ,  $k_{\mu_5,\text{eff}} = 2$  which could compromise the actual growth rate of  $B_{\text{rms}}$ . We will test that statement by varying the wave number of the sine function in series S.

### B. The role of the effective correlation length of $\mu_5$

The run S2 is now compared to run H1 with an initially constant  $\mu_5$  that has the same value as the amplitude of the sine spatial profile in S2, i.e.,  $\mu_{5,\max}$  in S2, and with the remaining runs of series S. In the latter, all runs are initialized with the same amplitude of  $\mu_5$  but different wave numbers; see Table I for details.

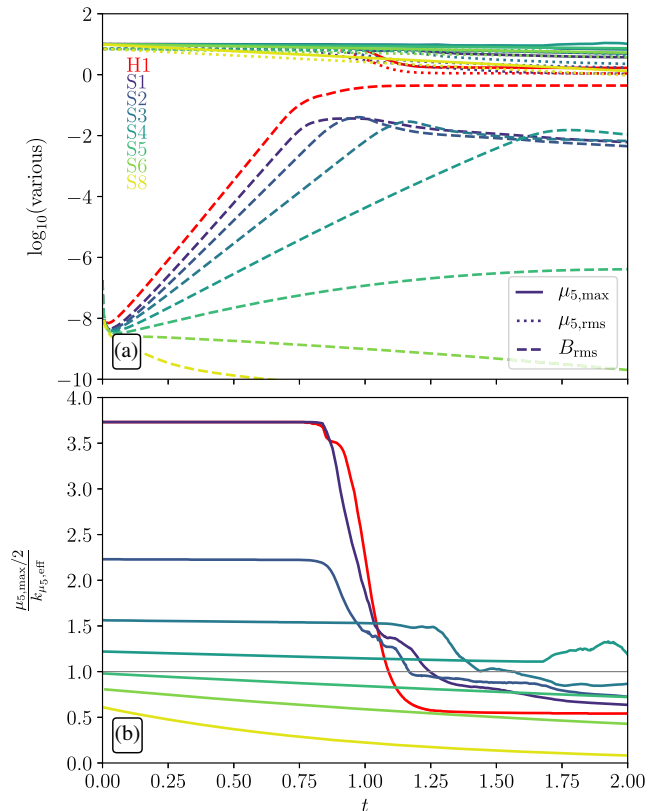


FIG. 3. Analysis for 2D runs from series S (and comparison run H1): (a) Time series of  $B_{\text{rms}}$ ,  $\mu_{\text{rms}}$ , and  $\mu_{\text{max}}$ . (b) Ratio of  $\mu_{5,\max}/2$  over  $k_{\mu_5,\text{eff}}$ .

The time evolution of  $B_{\text{rms}}$ ,  $\mu_{\text{rms}}$ , and  $\mu_{5,\max}$  for all runs from series S and run H1 is presented in Fig. 3(a). The largest growth rate is observed for run H1, but run S1 has only a slightly smaller growth rate. S1 has the lowest effective correlation length of  $\mu_5$  ( $k_{\mu_5,\text{eff}} \approx 1$ ). With increasing values of  $k_{\mu_5,\text{eff}}$ , the amplification of  $B_{\text{rms}}$  becomes slower. In runs S6 and S8,  $B_{\text{rms}}$  decays. In Fig. 3(b), the ratio of  $\mu_{5,\max}/2$  to  $k_{\mu_5,\text{eff}}$  is presented for all runs. Interestingly, an increase of  $B_{\text{rms}}$  by a factor of 10 is observed for S5, despite  $\mu_{5,\max}/(2k_{\mu_5,\text{eff}})$  being less than 1 from the initial time.

In particular, for runs with spatial sine profiles with high wave numbers, the growth rate of the  $v_5$  dynamo instability decreases due to a dissipation of  $\mu_5$ . Hyperdiffusion is applied in most runs of series S. Nevertheless, for runs that are set up with an inhomogeneity in  $\mu_5$  at high wave numbers, in particular for runs S4–S8, significant dissipation of  $\mu_5$  leads to a constantly decreasing  $\gamma_{\text{rms}}$ . The dissipation of  $\mu_5$  can also be seen in Fig. 4(a), where the value of  $\mu_{5,\max}/2$  is shown at different times as a function of  $k_{\mu_5,\text{eff}}$  (at  $t_0$ ) for all runs of series S and run H1. As long as  $\mu_{5,\max}/2 \ll k_{\mu_5,\text{eff}}$ , the observed dynamo growth rate should be close to the maximum theoretical value,  $\eta\mu_{5,\max}^2/4$ . Indeed, it can be seen in Fig. 4(b) that the observed growth rate (maximum value across the entire simulation time)

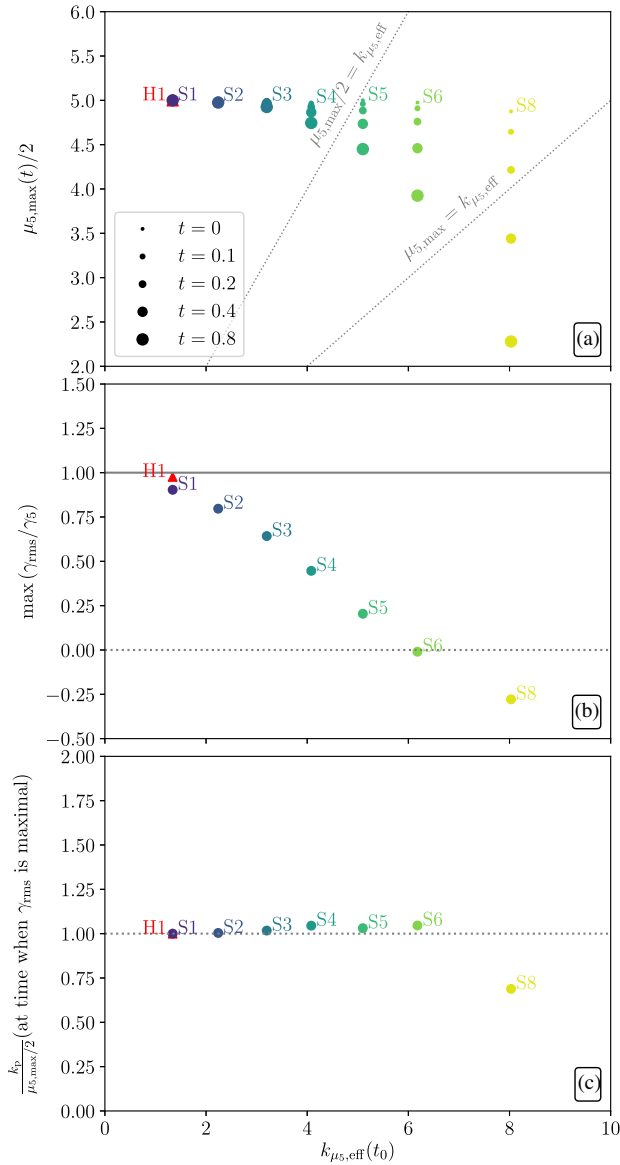


FIG. 4. Analysis for 2D runs from series S (and comparison run H1): Measured quantities vs the initial effective correlation length of  $\mu_5$ ,  $k_{\mu_5,\text{eff}}(t_0)$ . (a) The value of  $\mu_{5,\max}/2$  measured in DNS. The size of the symbols indicates time. For comparison the critical lines  $\mu_{5,\max}/2 = k_{\mu_5,\text{eff}}$  and  $\mu_{5,\max} = k_{\mu_5,\text{eff}}$  are presented. (b) The maximum (over the entire simulation time) of the measured growth rate  $\gamma_{\text{rms}}$ , normalized by  $\gamma_5$ . (c) The ratio of the peak of the magnetic energy spectrum,  $k_p$ , and  $\mu_{5,\max}/2$  at the time when the maximum growth rate is reached.

becomes smaller than  $\eta\mu_{5,\max}^2/4$  with increasing  $k_{\mu_5,\text{eff}}$ . Once  $\mu_{5,\max}$  drops below  $k_{\mu_5,\text{eff}}$ , no dynamo instability can occur, which is the case for runs S6 and S8. In all cases where a dynamo instability occurs, analysis of the magnetic energy spectra shows that the maximum growth rate is attained for the scale  $\mu_{5,\max}/2$ ; see Fig. 4(c). Even run S6, where the rms magnetic field never increases, shows a peak at  $\mu_{5,\max}/2$  at the time when  $\gamma_{\text{rms}}$  is maximum.

### C. Termination of growth caused by alternation of the spatial distribution of $\mu_5$

In this section we analyze the mechanism that limits the growth of the  $v_5$  dynamo. It differs from that where there is an initially nonvanishing  $\langle\mu_5\rangle$ . For an initial  $\mu_5$  with zero mean value and simultaneously vanishing  $\langle\mathcal{H}\rangle$ , the total chirality,  $\langle\mathcal{H}\rangle + 2\langle\mu_5\rangle/\lambda$ , which is the conserved quantity in the system, is zero and stays zero, except for noise related to numerical precision; see Fig. 1(a) where  $\langle\mathcal{H}\rangle + 2\langle\mu_5\rangle/\lambda$  grows initially but never reaches values above  $10^{-8}$ . Hence, the termination of further growth cannot be caused by  $\langle\mathcal{H}\rangle$  reaching a value comparable to  $2\langle\mu_5\rangle/\lambda$  which is the case for simulations with constant initial  $\mu_5$ , like for example H1.

Direct comparison of run H1 with series S in Fig. 3(a), shows that the  $v_5$  dynamo is much less efficient for runs with  $\langle\mu_5\rangle(t_0) = 0$ . The maximum of  $B_{\text{rms}}$  is smaller in all runs S than in run H1 by at least a factor of 10. Looking at Fig. 3(b), it appears that, in series S, the  $v_5$  dynamo reaches its maximum when the ratio of  $\mu_{5,\max}/2$  to  $k_{\mu_5,\text{eff}}$  drops to the order of 1, quenching the dynamo instability. The decrease of the ratio of  $\mu_{5,\max}/2$  to  $k_{\mu_5,\text{eff}}$  is largely caused by a change of the spatial structure of  $\mu_5$  which happens when the magnetic field grows and the  $\lambda$  term in Eq. (4) becomes important. By that time the spectrum  $E_5$  has changed significantly, leading to an increase of  $k_{\mu_5,\text{eff}}$ ; see Fig. 2(a) for an example.

The restructuring of the spectrum  $E_5$  and the accompanying increase of  $k_{\mu_5,\text{eff}}$  depends on the strength of the coupling between the magnetic field and the chiral chemical potential  $\mu_5$ . This strength of the coupling is controlled by the parameter  $\lambda$ . To test this hypothesis, we run two more simulations with the same initial conditions and the same parameters as in run S2, expect for the parameter  $\lambda$  which is decreased by a factor of  $10^2$  in run S2 $\lambda$ 2 and increased by the same factor in run S2 $\lambda$ 6. The results for these runs are presented in Fig. 5. Indeed, the run with the smallest  $\lambda$  (S2 $\lambda$ 2) reaches the highest  $B_{\text{rms}}$  while run S2 $\lambda$ 6 saturates at a value that is 10 times less. Figure 5(b) shows that the ratio  $\mu_{5,\max}/2$  over  $k_{\mu_5,\text{eff}}$  drops earlier for runs with larger  $\lambda$ . We note that, even though run S2 $\lambda$ 2 has a parameter  $\lambda$  that is  $10^2$  larger than the one for run H1, the dynamo with initially vanishing  $\langle\mu_5\rangle$  is still not as efficient as for a uniform distribution of  $\mu_5$ .

In Fig. 6, the time at which the dynamo reaches maximum energy is compared to the time at which  $\mu_{5,\max}/2$  becomes smaller than  $k_{\mu_5,\text{eff}}$  for all 2D runs from series S and H1. Here, dynamo limitation is defined as the time when  $\gamma_{\text{rms}}$  drops below  $10^{-4}$  which is more than 2 orders of magnitude below the maximum possible growth rate in the system,  $\eta\mu_5^2/4 = 2.5 \times 10^{-2}$ . All runs except for the ones which have initial small-scale  $\mu_5$  fields, S5, S6, and S7, and S2 $\lambda$ 2, lie on the linear correlation in Fig. 6. Regarding S2 $\lambda$ 2,  $k_{\mu_5,\text{eff}}$  never drops below  $\mu_{5,\max}/2$ ;

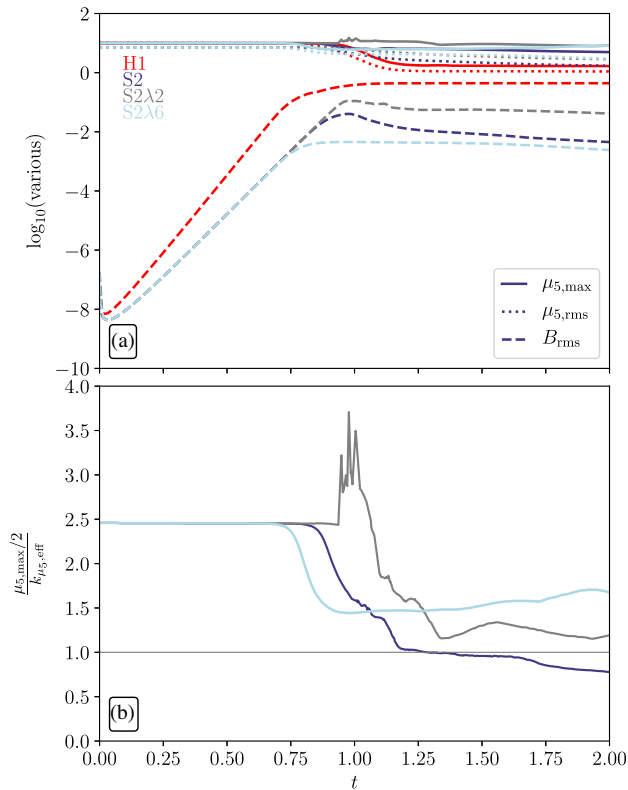


FIG. 5. Analysis for 2D runs from series S with an initial sine spatial profile with  $k = 2$  and different values of  $\lambda$  (and the comparison run H1). (a) Time series of  $B_{\text{rms}}$ ,  $\mu_{\text{rms}}$ , and  $\mu_{\text{max}}$ . (b) Ratio of  $\mu_{5,\max}/2$  to  $k_{\mu_5,\text{eff}}$ .

however at the time when the magnetic field reaches its maximum, the ratio  $(\mu_{5,\max}/2)/k_{\mu_5,\text{eff}}$  drops to  $\approx 1.1$ , possibly reducing the scale separation sufficiently to quench the  $v_5$  dynamo.

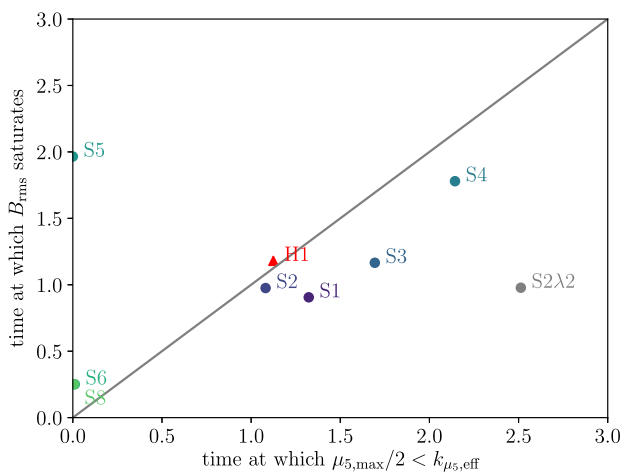


FIG. 6. Comparison between the time at which  $B_{\text{rms}}$  saturates and the time at which the chiral dynamo instability scale,  $\mu_{5,\max}/2$ , becomes smaller than  $k_{\mu_5,\text{eff}}$  for all 2D runs from series S and H1.

#### IV. MEAN-FIELD DYNAMOS DRIVEN BY AN INHOMOGENEOUS $\mu_5$

For a homogeneous initial  $\mu_5$ , the magnetic field generated by the  $v_5$  dynamo drives turbulence, which eventually causes mean-field dynamo action [21,26] if the plasma parameters are supercritical. Specifically, the criteria for the occurrence of a mean-field dynamo are as follows:

- (i) The Reynolds numbers have to be much larger than 1.
- (ii) The  $\lambda$  parameter should be small enough, so that  $\langle \mathbf{A} \cdot \mathbf{B} \rangle$  is still less than  $2\langle \mu_5 \rangle / \lambda$  at the time when turbulence sets in.

The objective of this section is to determine whether conditions (i) and (ii) can be satisfied in a plasma with an initially inhomogeneous  $\mu_5$  with zero mean and a mean-field dynamo can be excited. In particular the role of condition (ii), which regulates the dynamo limitation, is unclear for systems with an initial spatial profile of  $\mu_5$  as a sine function (3D runs from series S) or with fluctuations of  $\mu_5$  over an extended range of spatial scales (run series R). As before, the simulations with nonuniform initial  $\mu_5$  will be compared to a run in which the initial  $\mu_5$  is constant in space (run H2).

##### A. DNS of an initial $\mu_5$ with sine spatial profile

Run S23D is set up in a way that should allow the development of turbulence for an initial spatial profile of  $\mu_5$  in the form of a sine function with wave number 2. In comparison to the runs S1–S8, this run is performed in 3D space instead of 2D, it has higher resolution, and the magnetic resistivity and viscosity values are 5 times lower than in the 2D runs. To reach higher magnetic field strengths, and therefore higher fluid velocities in the simulation, the initial amplitude of the sine function is set to a value which is 5 times higher than in the 2D runs. In S23D, we have  $\mu_{5,\max} = 50$ , implying a characteristic wave number of the  $v_5$  dynamo instability of  $k_5 = 25$ . Furthermore, in comparison to the 2D runs in series S, the chiral feedback parameter  $\lambda$  is reduced to delay the back-reaction of  $\mathbf{B}$  on  $\mu_5$ . Both, the higher initial amplitude of  $\mu_5$  and the lower value of  $\lambda$  lead to an extended period of dynamo action and thereby higher magnetic field strengths. To test the importance of scale separation in the development of turbulence from an inhomogeneous chiral chemical potential, we perform a second high-resolution run with an initial  $\mu_5$  spatial profile in the form of a sine function with wave number  $k = 20$  (run S203D).

The time evolution of  $B_{\text{rms}}$  and other relevant quantities of run S23D are presented in Fig. 7(a). The high initial value of  $\mu_{5,\max}$  leads to the  $v_5$  dynamo instability that amplifies  $B_{\text{rms}}$  by approximately 8 orders of magnitude. Simultaneously,  $U_{\text{rms}}$  grows with twice the growth rate as the one of  $B_{\text{rms}}$  and the two fields become comparable at  $t \approx 0.03$ . At that time, the magnetic Reynolds number has

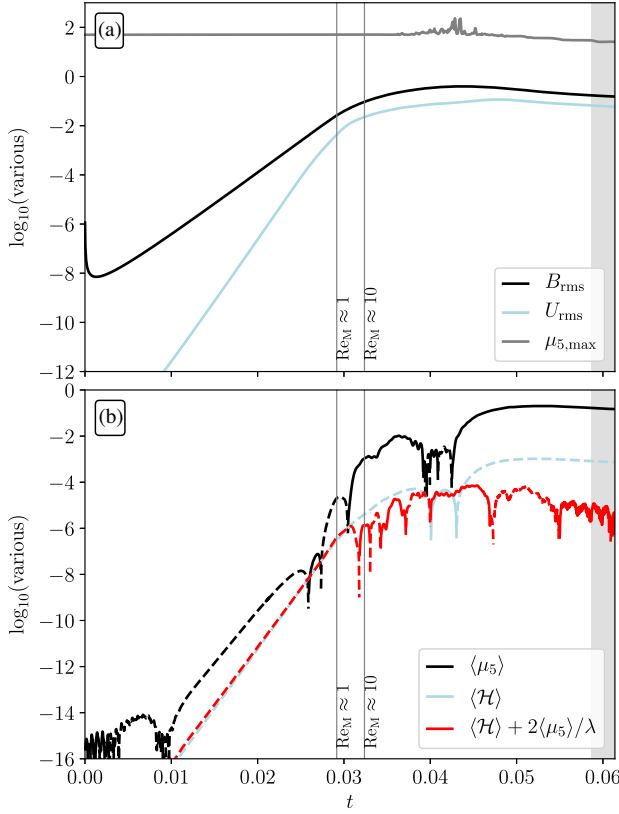


FIG. 7. Time evolution of run S23D. (a) The rms values of  $B$ ,  $U$ , and  $\mu_5$  as well as the maximum value of  $\mu_5$ . (b) The volume averages of  $\mu_5$  and  $A \cdot B$  and the conserved quantity in chiral MHD,  $\langle A \cdot B \rangle + 2\langle \mu_5 \rangle / \lambda$ . Here, a positive sign is indicated by solid line style and a negative sign by dashed line style.

become larger than unity, leading to the onset of turbulent effects. In run S23D, we have initially  $\langle \mu_5 \rangle = 0$ , and the mean magnetic field is not generated at the initial time. However,  $\langle \mu_5 \rangle$  is produced at approximately twice the rate of  $B_{\text{rms}}$ ; see Fig. 7(b). Until the time  $t = 0.027$ , the signs of both  $\langle \mu_5 \rangle$  and  $\langle A \cdot B \rangle$  are negative, but with the onset of turbulence, the signs of  $\langle \mu_5 \rangle$  and  $\langle A \cdot B \rangle$  are always opposite. Eventually,  $\langle \mu_5 \rangle$  reaches a value of  $+0.2$ , and hence a significant mean chiral chemical potential is produced. Due to numerical precision,  $\langle \mathcal{H} \rangle + 2\langle \mu_5 \rangle / \lambda$  grows to a value of  $\approx 10^{-5}$ , despite the opposite signs of  $\langle \mu_5 \rangle$  and  $\langle A \cdot B \rangle$ . We stress that  $\langle \mathcal{H} \rangle + 2\langle \mu_5 \rangle / \lambda$  only reaches values that are below the numerical precision and that this does not indicate a violation of the conservation law.

The evolution of the spatial structures of  $\mu_5$ ,  $A \cdot B$ , and  $B_x$  on the surface of the numerical domain, can be seen in Fig. 8. In the  $v_5$  dynamo phase (left column of Fig. 8), it can be seen that in regions where  $\mu_5 < 0$ , a negative  $A \cdot B$  is generated, and in regions where  $\mu_5 > 0$  also  $A \cdot B > 0$ . The magnetic field is generated on small spatial scales ( $k \approx 25$ ) which is consistent with the initial amplitude of the  $\mu_5$  sine function;  $\mu_{5,\max}(t_0) = 50$ . The fastest amplification of  $A \cdot B$

and  $B_x$  occurs in the regions where the amplitude of  $\mu_5$  has maxima. The spatial correlation between the signs of  $\mu_5$  and  $A \cdot B$  can still be seen in the nonlinear phase; see the middle column of Fig. 8 which shows the snapshots at  $t = 0.04$ . At this time, the characteristic scale of  $B_x$  has already increased significantly ( $k \approx 5$ ). The right-hand column of Fig. 8 shows the simulation at the time when the inverse cascade reaches the domain size, i.e., the first time when  $k_p = k_1$ . By this time, fluctuations in  $\mu_5$  have increased strongly and both,  $A \cdot B$  and  $B_x$ , exhibit a large-scale structure.

The evolution of the spatial structure in run S23D can also be seen in the power spectra at different times. Figure 9(a) shows the evolution of  $E_5(k, t)$  and Fig. 9(b) the one of  $E_M(k, t)$ . The magnetic energy peaks initially at  $k \approx 25$ , as expected from the  $v_5$  dynamo theory for an amplitude of  $\mu_{5,\max} = 50$ . However, the magnetic energy grows also at smaller wave numbers and obeys a  $k^4$  spectrum. After  $t \approx 0.03$ , the peak of  $E_M$  shifts towards larger spatial scales, i.e., smaller  $k$ . During that phase, the amplitude of  $E_M$  still increases and a magnetic spectrum  $E_M \propto k^{-3}$  is established, together with a spectrum of the chiral chemical potential  $E_5 \propto k^{-1}$ ; see Fig. 9. This is different from the case of a uniform  $\mu_5$  field, where the magnetic spectrum is  $E_M \propto k^{-2}$ . The amplitude of  $E_M$  decreases only after the inverse cascade has reached the initial scale of  $\mu_5$ ,  $k = 2$ . By the time when the inverse cascade arrives at the minimum wave number of the numerical domain,  $k = k_1 = 1$ , the  $E_M$  spectrum becomes less steep and is closer to  $k^{-2}$ . We note that, already at early times  $t < 0.03$ , the spectrum of the chiral chemical potential,  $E_5$ , also grows at  $k \approx 25$ ; see Fig. 9(a). At late times,  $E_5$  has been strongly modified by the magnetic field: the peak at  $k = 2$  has vanished and an almost flat spectrum towards large  $k$  has developed. The final scaling is approximately  $E_5 \propto k^{-1}$ .

We now analyze the amplification of the magnetic field on different scales in more detail. In particular, we compare the evolution of the magnetic field strength associated with the energy of magnetic fluctuations  $b$  at the wave number of the maximum growth rate of the  $v_5$  dynamo instability [57] with the one at the time-dependent integral scale of turbulence,  $k_{\text{int}}(t)$ :

$$\langle B \rangle_{\text{int}} \equiv \left[ \frac{\int_0^{k_{\text{max}}} E_M(k)^2 dk}{\int_0^{k_{\text{max}}} E_M(k) dk} \right]^{1/2}. \quad (20)$$

The time evolution of  $b \equiv [2 \int_{k_5}^{k_{\text{max}}} E_M(k) dk]^{1/2}$  and  $B_{\text{int}}$  is presented in Fig. 10(a). With the integral scale being  $k = 25$  during the  $v_5$  dynamo phase,  $b$  and  $B_{\text{int}}$  are identical for  $t \lesssim 0.03$ . At  $t \gtrsim 0.03$ ,  $b$  saturates while  $B_{\text{int}}$  continues to grow at a lower rate until  $t \approx 0.045$ . To understand the measured growth rates, we calculate the different contributions to the mean-field dynamo; see Fig. 10(b).

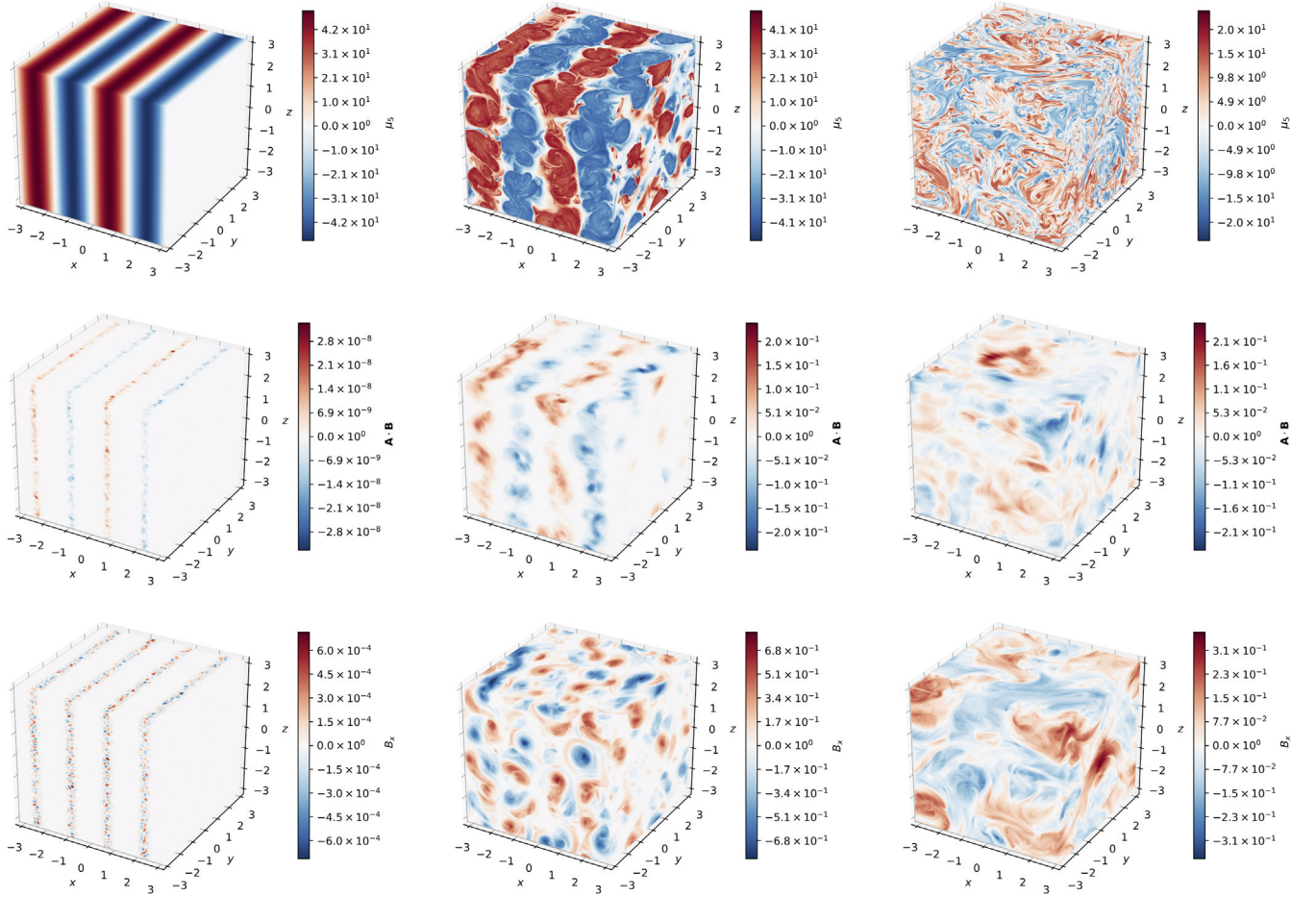


FIG. 8. Snapshots of run S23D taken at the different times: during the  $v_5$  dynamo phase ( $t = 0.02$ , left), the mean-field dynamo phase ( $t = 0.04$ , middle), and at the time when the inverse cascade reaches the scale of the domain ( $t = 0.06$ , right).

Further, positive and negative contributions to the mean-field dynamo growth rate are presented in Fig. 10(c).

The measured growth rate of the magnetic field strength on different scales is presented in Fig. 10(d). Note that the amplification at  $k = 25$  stops at  $t \approx 0.03$  but before that it is well described by  $\gamma_5$  as given by Eq. (6) with  $\mu_5 = \mu_{5,\max}$ . When the maximum field strength of the  $v_5$  dynamo is reached at  $k = 25$ , the amplification on larger scales becomes more prominent. However, it cannot clearly be ascribed to a mean-field dynamo since there the chiral chemical potential is decreasing, which leads to a decrease of the characteristic instability wave number,  $k_5(t) = \mu_{5,\max}(t)/2$ . To investigate the role of the mean-field dynamo in the amplification of energy on large spatial scales, we plot the different contributions in Fig. 10(b): the mean  $v_5$  based on the integral scale of turbulence,  $\alpha_M$  based on the correlation time of fluctuations on  $k_{\text{int}}$  as well as the steady state value of the magnetic  $\alpha$  effect,  $\alpha_M^{\text{sat}}$ . We also show that  $\alpha_\mu$ , based on Eq. (11), changes sign at  $t \approx 0.03$ . The dominant contribution to the mean-field dynamo is the magnetic  $\alpha$  effect. We also compare the measured growth rate after  $t \approx 0.03$ . The theoretical curve,  $\gamma_\alpha$ , describes

roughly the measured growth rate based on averaging over the integral scale,  $\gamma_{\text{int}}$ , for  $0.035 \lesssim t \lesssim 0.045$ .

Note, that the magnetic Reynolds number increases throughout both the  $v_5$  dynamo phase and also the mean-field dynamo phase, because (i) the velocity field continues to grow and (ii) the wave number based on the integral scale of turbulence decreases. Therefore, the turbulent diffusion  $\eta_T = \text{Re}_M \eta / 3$  increases continuously and eventually the decay term  $(\eta + \eta_T)k^2$  dominates over the source term  $(\bar{v}_5 + \alpha)k$  in Eq. (16). When this equilibrium is reached at the minimum wave number of the domain,  $k_1 = 1$ , the mean-field dynamo would operate only on scales beyond the numerical domain and the amplification of  $\langle B \rangle_{\text{int}}$  comes to an end. Indeed, turbulent magnetic diffusion for the minimum wave number,  $\eta_T$ , becomes larger than  $|\alpha_M^{\text{sat}}|$  at  $t \approx 0.048$  [see Fig. 10(c)], at which time the measured  $\gamma_{\text{int}}$  has dropped below zero.

In Fig. 11, a direct comparison between the high-resolution run with constant initial  $\mu_5$  (run H2) and inhomogeneous  $\mu_5$  (run S23D) is presented. In both cases, the ratio of  $\langle B \rangle_{\text{int}}$  and the magnetic field  $B_5$  related to the  $v_5$  dynamo, starts increasing at the onset of the mean-field

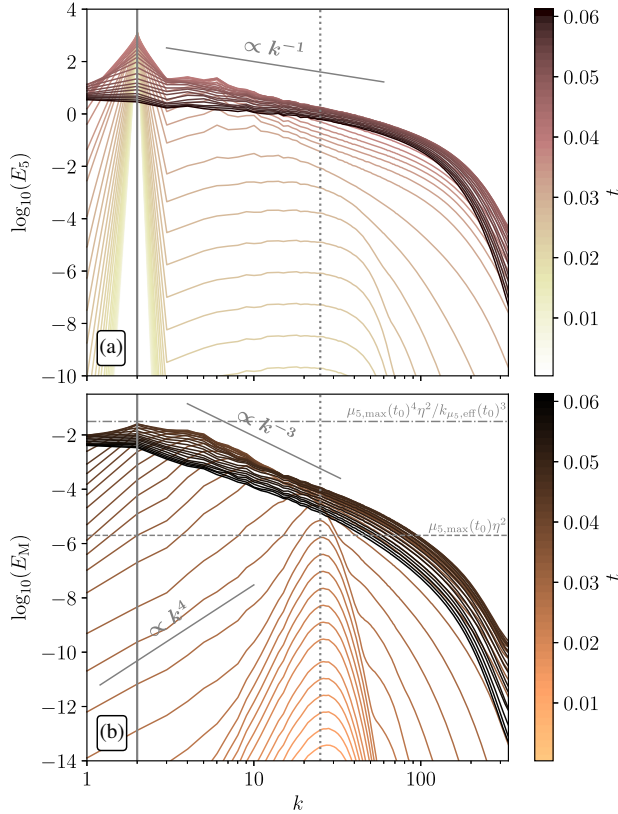


FIG. 9. Evolution of power spectra in Run S23D. (a) Power spectra of  $\mu_5$ ,  $E_5$ . (b) Magnetic energy spectra,  $E_M$ . The horizontal lines indicate the level of  $E_M$  at the onset of the inverse cascade (gray dashed line; as discussed in Ref. [25]) and the maximum energy (gray dashed-dotted line; see Sec. IV E).

dynamo; see Fig. 11(a). For H2, the mean-field dynamo starts at  $t \approx 0.04$  and for S23D at  $t \approx 0.03$ . The mean-field dynamo phase in run S23D begins earlier, since its initial maximum value of  $\mu_5$  is larger than the one in H2 [ $\mu_{5,\max}(t_0) = 42$  for H2 and  $\mu_{5,\max}(t_0) = 50$  for S23D; see Table I]. This leads to a higher growth rate of the magnetic field, as can be seen in Fig. 11(b), and therefore to a faster generation of turbulence in the system. Qualitatively, the growth rates of magnetic energy on different wave numbers evolve in a similar way in H2 and S23D. The growth rate on the characteristic instability scale of the  $v_5$  dynamo,  $\gamma_5$ , and the one on the integral scale of turbulence,  $\gamma_{\text{int}}$ , are comparable during the  $v_5$  dynamo phase. With the onset of turbulence,  $\gamma_5$  drops to zero while  $\gamma_{\text{int}}$  decreases but remains positive for an extended time.

In S203D, the magnetic field on the integral scale never becomes larger than the rms value; see the red line in Fig. 11(a). Here, the growth rate in the  $v_5$  dynamo phase is less than in S23D by a factor of more than 2. This is consistent with the findings in Sec. III B, where the  $v_5$  dynamo could not develop well in setups with effective correlation wave numbers  $k_{\mu_5,\text{eff}}$  that were close to the dynamo instability scale  $k_5$ ; see also the power spectra for

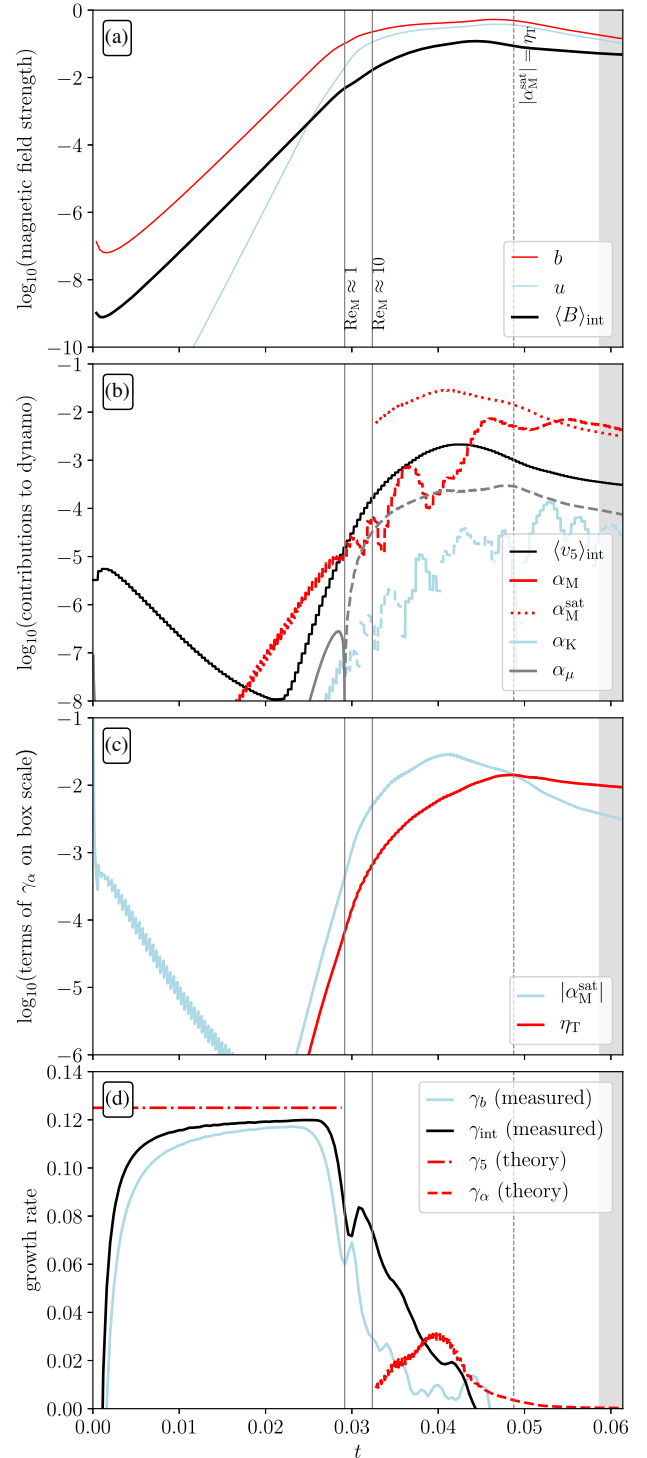


FIG. 10. Evolution of run S23D. (a) Time series of  $\langle B \rangle_{\text{int}}$ ,  $b$ , and  $u$ . (b) Different contributions to the mean-field dynamo: the mean chiral velocity  $\langle v_5 \rangle_{\text{int}}$  and different estimates of the  $\alpha$  effect. A positive sign is indicated by solid line style and a negative sign by dashed line style. (c) The two terms of the mean-field dynamo growth rate. (d) The measured growth rate of  $\langle B \rangle_{\text{int}}$  and  $b$  and comparison with the theoretical predictions for the nonturbulent dynamo phase at  $t \lesssim 0.028$  and the turbulent mean-field dynamo phase,  $t \gtrsim 0.032$ . Note, that  $\gamma_\alpha$  is based on the largest contribution to the mean-field dynamo,  $\alpha_M$ .

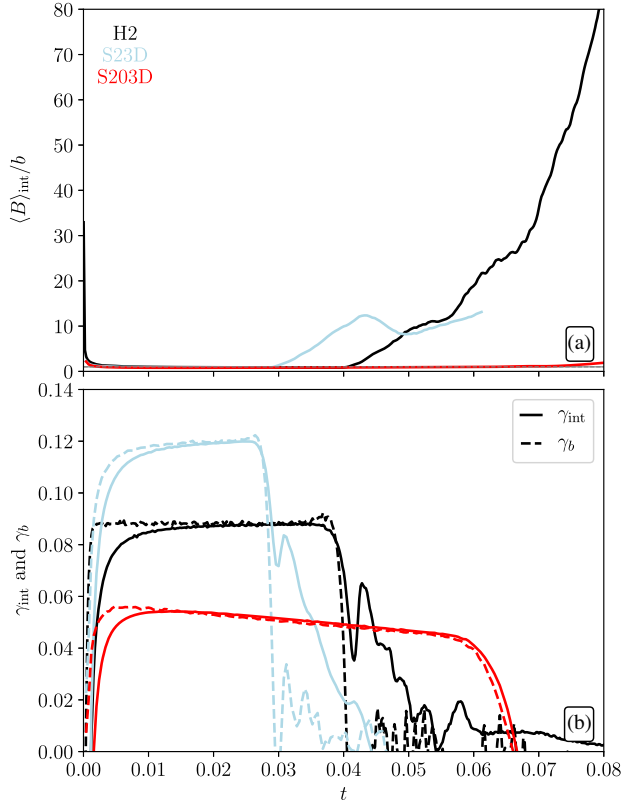


FIG. 11. Time evolution of the magnetic field in runs H2, S23D, and S203D. (a) Ratio of the magnetic field strength on the integral scale of turbulence,  $\langle B \rangle_{\text{int}}$ , and the strength of fluctuations,  $b$ . (b) The measured growth rates of  $\langle B \rangle_{\text{int}}$  (solid lines) and  $b$  (dashed lines).

run S203D in Figs. 22(c) and 22(d) shown in Appendix C. The growth rate in S203D even decreases during the  $v_5$  dynamo phase due to diffusion at the high wave number  $\mu_5$ . At  $t \approx 0.06$ , both  $\gamma_5$  and  $\gamma_{\text{int}}$  drop to zero in run S203D, therefore indicating no sign of a mean-field dynamo. In fact, turbulence never develops in S203D and the maximum  $\text{Re}_M$  over the entire simulation time is only 2.06; see Table I.

### B. DNS with initial fluctuations of $\mu_5$

This section complements Ref. [48], in which we have analyzed DNS with an initially random distribution of  $\mu_5$ . The existence of a mean-field dynamo phase in these scenarios has been reported in Ref. [48] as the first demonstration of the generation of large-scale magnetic fields from an  $\mu_5$  with initially vanishing mean value. In this section, we analyze the properties of this instability in greater and more technical details.

As a reference run for a DNS with initial random distributions of  $\mu_5$  we use run R-2 and begin with a direct comparison to our previous example of a sine function initial spatial profile of  $\mu_5$ , run S23D. Snapshots of  $\mu_5$ ,  $A \cdot B$ , and  $B_x$  of run R-2 at different

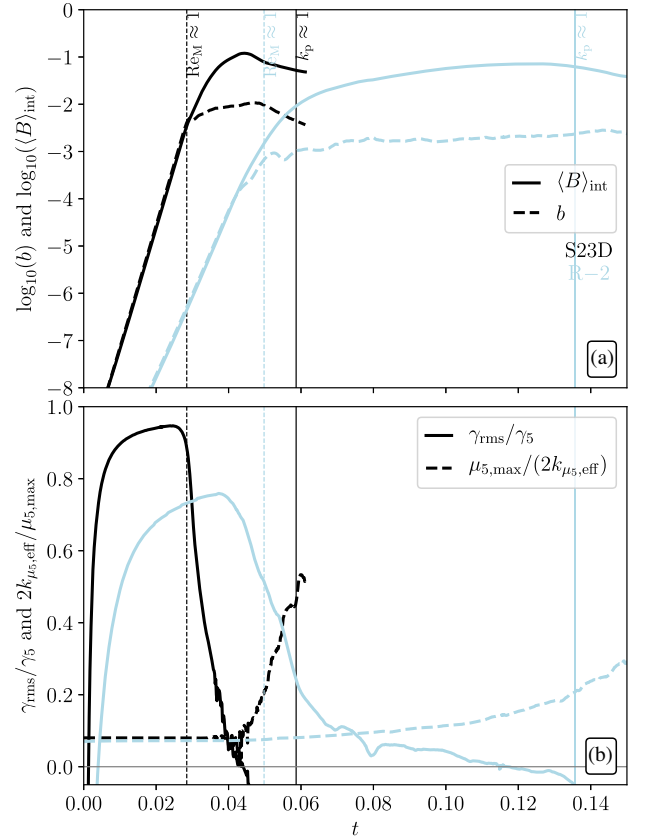


FIG. 12. Direct comparison between the reference run with an initial  $\mu_5$  in the form of a sine spatial profile in the  $x$  direction, S23D, and the reference run with random fluctuations of  $\mu_5$ , R-2. (a) Time evolution of  $\langle B \rangle_{\text{int}}$  and  $b$ . (b) Growth rate of  $B_{\text{rms}}$  normalized by  $\gamma_5$  and the ratio of  $\mu_{5,\text{max}}/2$  and  $k_{\mu_5,\text{eff}}$ .

times are presented in the Appendix B; see Fig. 21. As shown in Fig. 12, the magnetic field growth in the  $v_5$  dynamo phase in R-2 is slower than in S23D despite the initially comparable values of  $\mu_{5,\text{max}}$ . The difference in growth rates in the two runs cannot be explained by different separation of scales. The ratio of the scale of the  $v_5$  dynamo instability,  $\mu_{5,\text{max}}/2$ , and the effective correlation length of  $\mu_5$ ,  $k_{\mu_5,\text{eff}}$ , is  $\approx 0.1$  in both runs. Therefore, the differences must come from the shape of the  $\mu_5$  spectra; see the spectra of R-2 in Fig. 13 and the one of S23D in Fig. 9. Note, that the measured growth rate in R-2 increases more slowly than in S23D, so for a lower value of the initial magnetic seed field, the maximum ratio of  $\gamma_{\text{rms}}/\gamma_5$  could get closer to 1. Another interesting difference between S23D and R-2 is the fact that the mean-field dynamo phase starts earlier in the latter run and also lasts longer. In S23D,  $\text{Re}_M > 10$  at  $t \approx 0.032$  and the maximum magnetic field is reached at  $t \approx 0.04$ . In R-2, the turbulent dynamo operates between  $t \approx 0.068$  and  $t \approx 0.12$  (see below).

The detailed mean-field dynamo analysis for R-2 is presented in Fig. 14. At  $t \approx 0.052$ , the magnetic Reynolds

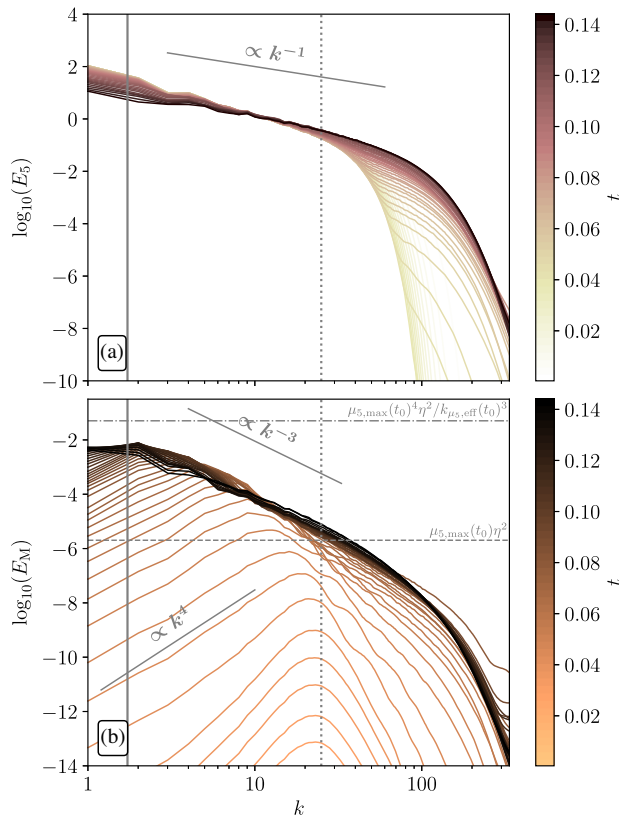


FIG. 13. Similar to Fig. 9, but for Run R – 2.

number becomes larger than unity, which coincides with the time when the magnetic energy at  $k = 25$  saturates; see Fig. 14(a). The magnetic field on the integral scale of turbulence,  $B_{\text{int}}$ , continues to grow with the predominantly positive contribution to the growth rate being the magnetic  $\alpha$  effect; see Fig. 14(b). As in run S23D, the maximum field strength of the mean-field dynamo occurs once  $\eta_T k^2$  becomes larger than  $|\alpha_M^{\text{sat}}|k$  at  $k = 1$ , based on the size of the numerical domain. This time is indicated by the vertical dashed lines in Fig. 14. We stress again, that the mean-field dynamo limitation is here primarily an effect of the finite size of the numerical domain: with increasing  $\text{Re}_M$ , the value of  $\eta_T$  and therefore, the characteristic wave number of the mean-field dynamo eventually become less than the minimum wave number of the domain. The growth rate during the mean-field dynamo phase,  $\gamma_\alpha$ , matches the measured growth rate of the magnetic field on the integral scale well between the time when  $\text{Re}_M > 10$  (vertical solid line at  $t \approx 0.068$ ) and the time when  $\eta_T = |\alpha_M^{\text{sat}}|$  (vertical dashed line at  $t \approx 0.117$ ).

### C. Comparison of mean-field dynamos in DNS with different initial $\mu_5$

Evidence for mean-field dynamos after the onset of turbulence exists for all DNS presented in this study that reach sufficiently high Reynolds numbers. A summary of

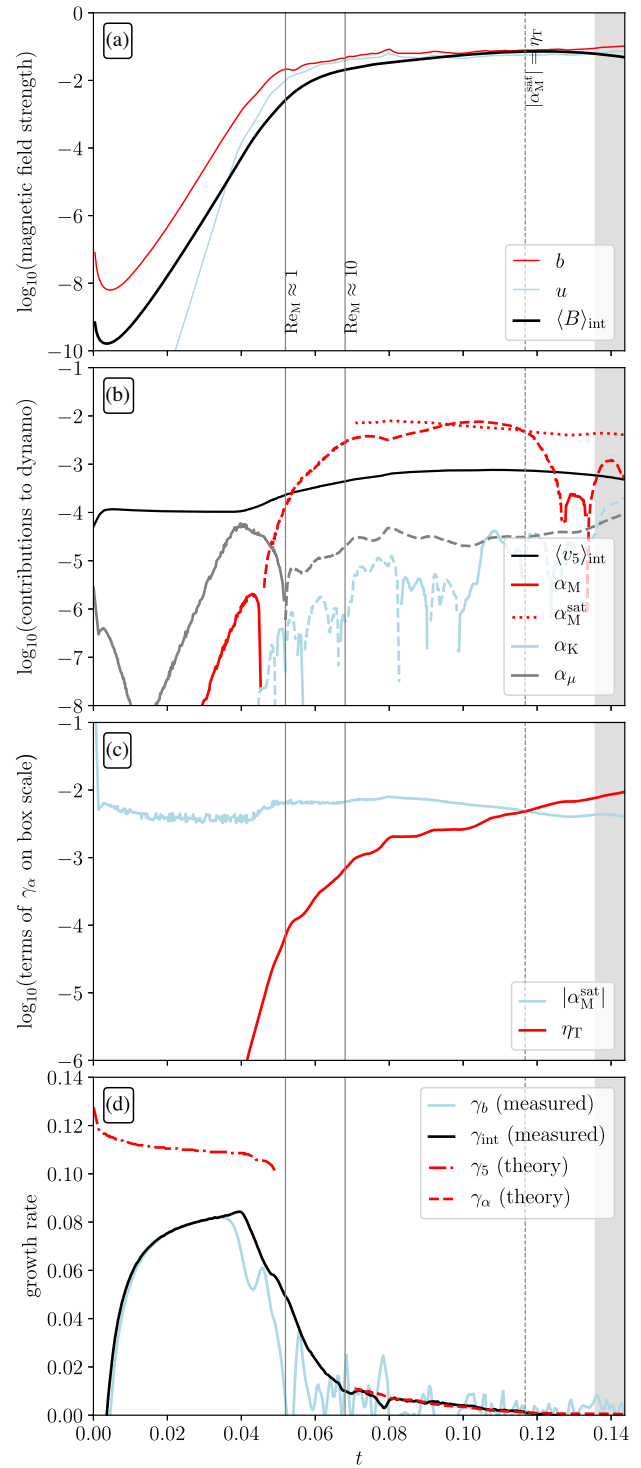


FIG. 14. Same as Fig. 10 but for run R – 2.

the measured growth rates in all DNS after the onset of turbulence, is presented in Fig. 15. There, blue lines show the growth rate of the characteristic magnetic field strength on the instability scale of the  $v_5$  dynamo, i.e., the growth rate of magnetic fluctuations  $\gamma_b$ . Since the time axes start at the moment when  $\text{Re}_M$  has become larger than unity,  $\gamma_b$  quickly drops to zero in all cases, but it keeps fluctuating in

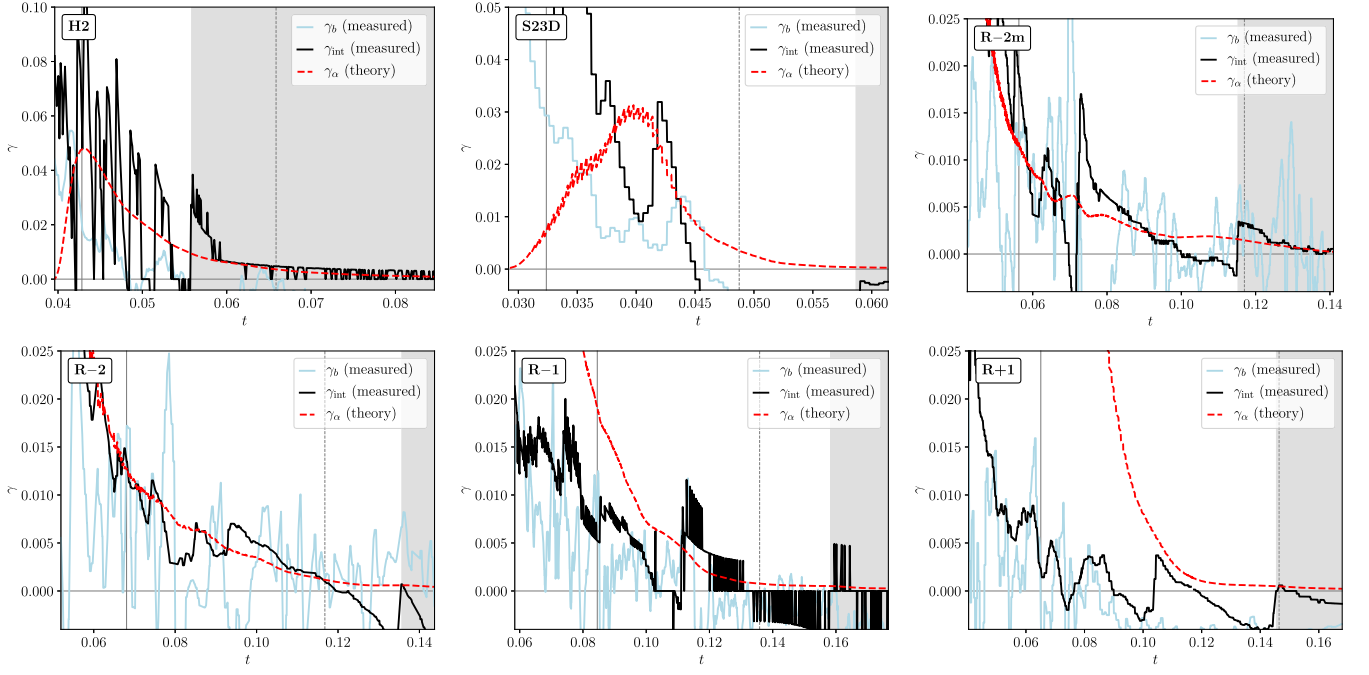


FIG. 15. Comparison between the measured growth rate and the theoretical prediction for all runs with turbulence. The blue lines show the growth rate of the magnetic field on the characteristic scale of the  $v_5$  dynamo and the black lines the rate on the integral scale of turbulence,  $k_{\text{int}}$ . The red dashed lines show the theoretically predicted growth rate of the mean-field dynamo,  $\gamma_\alpha$ . In the case of H2,  $\gamma_\alpha = \alpha_\mu^2 / (4\eta_T)$ , while for all other runs,  $\gamma_\alpha = (\alpha_M^{\text{sat}})^2 / (4\eta_T)$ . The time axes start at the moment when  $\text{Re}_M = 1$  and the solid vertical lines indicate the time when  $\text{Re}_M = 10$ . The dashed vertical lines show the time when  $|\alpha_M^{\text{sat}}| < \eta_T$  (and  $|\alpha_\mu| < \eta_T$  for run H2), i.e., when the characteristic scale of the mean-field dynamo has increased to a length that is larger than the size of the numerical domain and therefore growth in DNS comes to an end. For times larger than  $t_{k_1}$ , i.e., when the peak of the magnetic energy spectrum has reached the wave number  $k_1$ , the plots are shaded in gray.

time. The black lines show the measured growth rates on the integral scale,  $\gamma_{\text{int}}$ , which decreases more slowly than  $\gamma_b$  in all runs. The theoretically expected growth rate of the mean-field dynamo,  $\gamma_\alpha$ , is shown as dashed red lines.

In the theoretical curves of  $\gamma_\alpha$ , we use the maximum contributions to the dynamo growth rate. In the case of run H2, the maximum contribution comes from the  $\alpha_\mu$  effect for which we use Eq. (11) with  $\langle v_5 \rangle = \eta \langle \mu_5 \rangle$ . Note that here the volume average  $\langle \mu_5 \rangle$  is larger than the average based on the integral scale of turbulence  $\langle \mu_5 \rangle_{\text{int}}$ . In agreement with previous findings reported in Ref. [26], the  $\alpha_\mu$  effect describes the growth rate of the mean-field dynamo in a system with a constant (homogeneous) initial  $\mu_5$  well.

The mean-field dynamo in all runs with an inhomogeneous initial  $\mu_5$  is best described by the magnetic  $\alpha$  effect, as given by Eq. (15). This has been discussed in detail for runs S23D and R-2 before, and is shown in Fig. 15 for all other runs with high  $\text{Re}_M$ .

In all runs, except for run H2, we have used  $\langle \mu_5 \rangle_{\text{int}}$  in the analysis of the mean-field dynamo. Like for runs S23D [Fig. 10(b)] and R-2 [Fig. 14(b)],  $\alpha_M$  is the dominant contribution in all runs with an inhomogeneous initial  $\mu_5$ . In the postprocessing of those runs, we have used  $\alpha_M^{\text{sat}}$ , taking averages of  $\mu_5$  and  $\mathbf{B}$  on the integral scale of turbulence

[58], to calculate  $\gamma_\alpha$ . For runs S23D, R-2m, R-2, and R-1, the theoretically expected  $\gamma_\alpha$  match the observed growth rate on the integral scale of turbulence,  $\gamma_{\text{int}}$ . For run R+1,  $\gamma_\alpha$  is much larger than  $\gamma_{\text{int}}$ , yet they seem to vanish at the same time  $t \approx 0.12$ . This mismatch in R+1 is probably due to the low value of the magnetic Reynolds number which only reaches  $\text{Re}_M \approx 16$  at its maximum.

#### D. Coevolution of power spectra

During the chiral dynamo phase, the power spectra of magnetic energy and the chiral chemical potential evolve in an interdependent way. When the magnetic energy grows for the wave number  $k_5$ ,  $E_5$  is also amplified around that wave number. This can be seen clearly in Fig. 9, where  $E_M$  is initially only concentrated at one wave number  $k = 2$  that coincides with the wave number of the initial sine profile of  $\mu_5$ . The amplitude of the sine function,  $\mu_{5,\text{max}} = 50$ , is large enough to cause an instability in the magnetic energy spectrum at  $k = 25$ . Figure 9(a) shows that also  $E_5$  grows on  $k = 25$  but with a broader peak. With the onset of the inverse cascade a power-law scaling in  $E_M$  develops and likewise a power-law slope in  $E_5$  is established first for  $k > 2$  and later also for the lowest wave numbers in the system. In the example of run S23D, we

observe a coevolution of the slopes of the power spectra  $E_M$  and  $E_5$ . Such a simultaneous change of slopes can also be seen for run R-2, the spectra of which are presented in Fig. 13.

To quantify the evolution of the  $E_M$  and  $E_5$  spectra, we determine their slope  $n$  by fitting to a power law  $\propto k^n$ . The fits are performed for all spectra after the onset of the inverse cascade at time  $t_{IC}$ , i.e., once the peak of  $E_M$ ,  $k_p$ , has become less than  $k_5$ . Since the power law typically extends to wave numbers larger than  $k_5$ , we set the fitting range at time  $t$  to  $k_p(t) < k < 2k_p(t_{IC})$ , where  $k_p(t)$  is the wave number at which  $E_M$  has its current maximum and  $k_p(t_{IC})$  is the wave number at which  $E_M$  had its maximum at the onset of the inverse cascade. Note, that  $k_p(t_{IC}) \approx k_5$ . To obtain a typical error, we divide the fitting range into three equidistant parts, fit these parts separately to obtain three fitting results  $n_1$ ,  $n_2$  and  $n_3$ . As the error we use  $\pm \max(|n_1 - \bar{n}|, |n_2 - \bar{n}|, |n_3 - \bar{n}|)$  with  $\bar{n} = (n_1 + n_2 + n_3)/3$ .

The time evolution of the power-law slopes in the  $E_M$  and  $E_5$  spectra after the onset of the chiral inverse cascade are presented in Fig. 16. Here, the results for all DNS with sufficiently high Reynolds numbers are shown. We find that the slopes evolve in an interdependent way for all cases, except for run R+1. In this case, the slopes evolve self-similarly only after the maximum magnetic field strength has been reached (i.e., after  $t \approx 0.1$ ). The reason for this is probably related to the original positive slope of the  $E_5$  spectrum, which requires a longer time for rearrangement to develop a negative slope and to follow the  $E_M$

spectrum. The time evolution of the power spectra of run R+1 is presented in the middle panels of Fig. 22, along with the spectra of run H2 (left panels) and run S203D (right panels), see Appendix C.

The setup with a random inhomogeneous  $\mu_5$  distribution with zero mean results in a  $\propto k^{-3}$  magnetic energy scaling, which is different from the case with a homogeneous  $\mu_5$  distribution, where the scaling is  $\propto k^{-2}$ . The two setups are rather different and have very different underlying physics. The principal difference is the following. In the linear stage of the chiral dynamo instability, an initially homogeneous  $\mu_5$  excites a magnetic field with a wave number whose value is around the average of  $\mu_5/2$  [see Fig. 22(b)], while a random  $\mu_5$  with zero mean excites a random magnetic field over a broad range of scales [see e.g. Fig. 13(b)]. In the nonlinear stage, there is an inverse cascade of the magnetic field and a magnetic driving of turbulence in both setups. However, the properties of turbulence in both systems are distinct from each other, as discussed next.

One of the indications of the difference in these systems is that there are two different mechanisms of generation of a mean-field dynamo in the resulting turbulent flows: (i) in the case of an initial homogeneous  $\mu_5$ , it is the  $\alpha_\mu$  effect related to the interactions of fluctuations of  $\mu_5$  and tangling magnetic fluctuations; (ii) in the case of a random  $\mu_5$  with zero mean, it is the magnetic  $\alpha$  effect, which is caused by the current helicity of small-scale magnetic fluctuations. Both types of  $\alpha$  effect are caused by the produced turbulence with different properties in both systems,

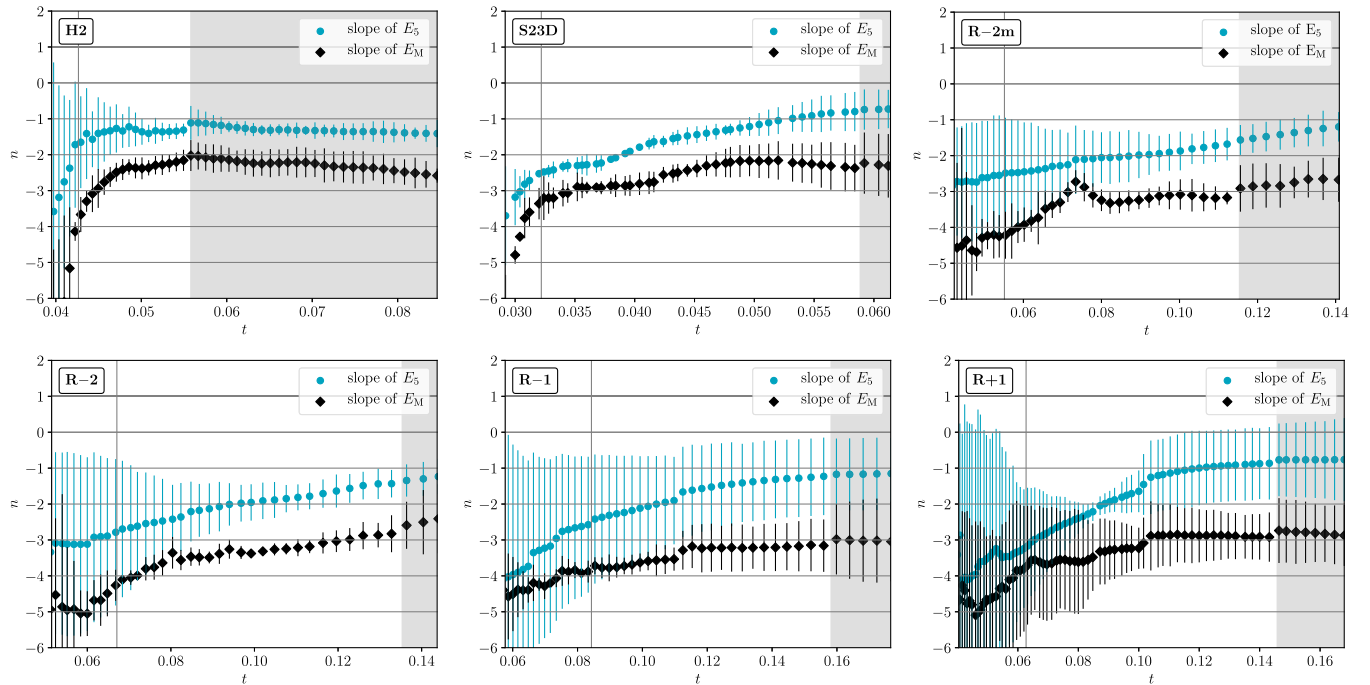


FIG. 16. Fitted slopes of the  $E_M$  and  $E_5$  spectra as a function of time for all runs with turbulence. The time axes start at the moment when  $Re_M = 1$  and the solid vertical lines indicate the time when  $Re_M = 10$ . For times larger than  $t_{k_1}$ , i.e., when the peak of the magnetic energy spectrum has reached the wave number  $k_1$ , the plots are greyed out.

resulting in different magnetic spectra in the final stage of the magnetic field evolution in these systems.

### E. Maximum field strength

The observed  $k^{-3}$  scaling of the magnetic energy spectra allows to estimate the maximum magnetic field strength. Assuming that it is controlled by  $\eta$  and  $\mu_{5,\max}(t_0)$ , dimensional arguments imply that the magnetic energy spectrum is given by

$$E_M(k) = C\bar{\rho}\eta^2[\mu_{5,\max}(t_0)]^4k^{-3}, \quad (21)$$

where  $C$  is a constant, and  $\bar{\rho} = 1$  in our DNS. We use  $C = 1$  for an order-of-magnitude estimate. The DNS indicate that the maximum value of  $E_M(k)$  is typically reached at the wave number  $k \approx k_{\mu_5,\text{eff}}(t_0)$  and therefore the maximum possible magnetic field is given by

$$B_{\text{sat,eff}} \approx \sqrt{2}\eta \frac{[\mu_{5,\max}(t_0)]^2}{k_{\mu_5,\text{eff}}(t_0)}. \quad (22)$$

For Eq. (22) it is assumed that  $k_{\mu_5,\text{eff}}$  does not change significantly during the dynamo instability. This is only a valid assumption if  $\lambda$ , i.e., the coupling between  $\mu_5$  and  $\mathbf{B}$ , is small. For large values of  $\lambda$ , there is a strong backreaction on the  $\mu_5$  field and the dynamo limitation occurs through the same mechanism as observed in the DNS of Ref. [25], i.e., by means of the conservation law:

$$B_{\text{sat},\lambda} \approx \frac{\mu_{5,\max}(t_0)}{\sqrt{\lambda}}. \quad (23)$$

In Fig. 17 we compare the maximum value of the rms magnetic field strength in the two phenomenological estimates given in Eqs. (22) and (23). The limitation mechanism via the conservation law plays a role for runs S23D $\lambda$ 4 and S23D $\lambda$ 8, while in the remaining runs, dynamo limitation is controlled by the initial correlation length of  $\mu_5$ .

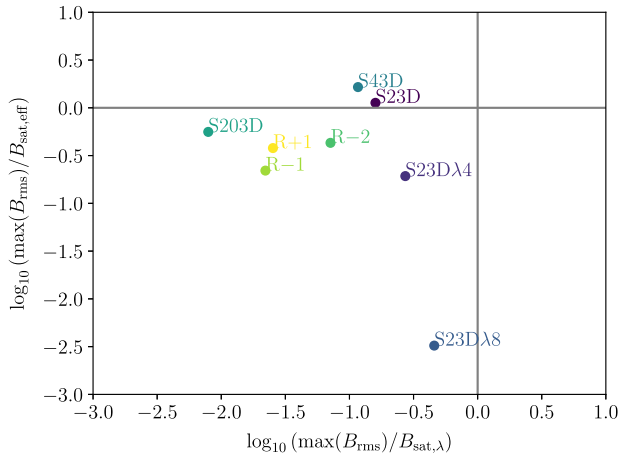


FIG. 17. Maximum magnetic field strength obtained in DNS over the  $B_{\text{sat,eff}}$  vs maximum magnetic field strength obtained in DNS over the  $B_{\text{sat},\lambda}$ .

### F. Effects of chiral magnetic waves

In this study, we have focused on scenarios where the dynamics is driven by the CME. However, there is also the chiral separation effect that describes the coupling between  $\mu_5$  and the chemical potential  $\mu = \mu_R + \mu_L$ . In the presence of an equilibrium mean magnetic field  $\mathbf{B}_0$ , a nonzero  $\mu$  permits chiral magnetic waves (CMWs) [50] with the frequency

$$\omega_{\text{CMW}} = (C_5 C_\mu)^{1/2} |\mathbf{k} \cdot \mathbf{B}_0|, \quad (24)$$

where  $C_5$  and  $C_\mu$  are coupling constants. The behavior of CMWs for an initial nonuniform random  $\mu_5$  has not yet been studied. To test the effects of CMWs on the scenario of chiral plasma instabilities driven by a nonuniform  $\mu_5$ , we perform two additional simulations that take the coupling to  $\mu$  into account. Therefore, Eq. (4) is replaced by

$$\frac{D\mu_5}{Dt} = \mathcal{D}_5(\mu_5) + \lambda\eta[\mathbf{B} \cdot (\nabla \times \mathbf{B}) - \mu_5 \mathbf{B}^2] - C_5(\mathbf{B} \cdot \nabla)\mu, \quad (25)$$

which we solve together with Eqs. (1)–(3) and the evolution equation for the chemical potential

$$\frac{D\mu}{Dt} = D_\mu \Delta \mu - C_\mu(\mathbf{B} \cdot \nabla)\mu_5. \quad (26)$$

We repeat run R-2 with the additional  $\mu$  dynamics. As an initial condition for  $\mu$  we use a uniform value of  $\mu = 51$ , which corresponds roughly to the initial maximum value of  $\mu_5$ . This initial condition implies that in grid cells where  $\mu_5 = 51$ , all fermions have the same handedness. For the coupling constants we use  $C_5 = C_\mu = 0.1$  in run R-2\_CMW1, which implies that the velocity of the CMW is roughly ten percent of the Alfvén velocity. For run R-2\_CMW2, we use  $C_5 = C_\mu = 1$ , so the velocity of the CMW is approximately equal to the Alfvén velocity. We note that for run R-2\_CMW2 we have used shock viscosity during the nonlinear phase for numerical stability. This means that we add a bulk viscosity  $\zeta = C_{\text{shock}} \delta x^2 \langle \max(0, -\nabla \cdot \mathbf{U}) \rangle$  to the stress tensor so that  $\tau_{ij} = 2\nu\rho\mathcal{S}_{ij} + \rho\zeta\delta_{ij}\nabla \cdot \mathbf{U}$ . Here, angled brackets denote a five-point running average. The technique of shock viscosity was developed by von Neumann and Richtmyer [59]; see Ref. [60] for an application to simulations of detonations with the Pencil Code.

Our two exemplary simulations with chiral magnetic waves show that they do not alter the dynamics of the systems presented in this work (see Figs. 18 and 19). The main reason is that these systems do not have an external magnetic field. Therefore, waves can only develop at late phases of the simulations. However, both runs, R-2\_CMW1 and R-2\_CMW2, do not show significant differences to run R-2 without  $\mu$ . As can be seen in Fig. 18, the maximum value of  $\mu_5$  decreases a bit faster when CMWs occur. Yet this does

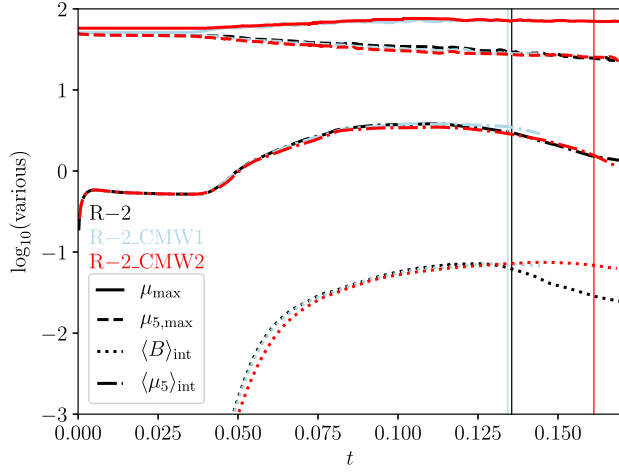


FIG. 18. Comparison of the time evolution of runs without (run R-2) and with (runs R-2CMW1 and R-2CMW2) the evolution of the chemical potential. The dynamics in all three runs are very comparable. Small differences can only be seen at late times, when a large enough  $\langle B \rangle_{\text{int}}$  has been produced that leads to chiral magnetic waves. The thin vertical lines with colors referring to the different runs indicate the time  $t_{k_1}$ .

not affect the production of the mean magnetic field  $\langle B \rangle_{\text{int}}$  significantly. In all three cases,  $\langle B \rangle_{\text{int}}$  grows up to approximately 0.1 by the time the inverse cascade reaches the minimum wave number of the numerical domain. Throughout the simulations, the maximum value of  $\mu$ ,  $\mu_{\text{max}}$  continuously grows in time. In Fig. 19, we demonstrate that also the magnetic energy spectra and the  $\mu_5$  spectra,  $E_M$  and  $E_5$ , at the time  $t_{k_1}$  are not significantly affected by the presence of CMWs. For the runs with  $\mu$  evolution, the  $\mu$  spectra,  $E_\mu$ , are comparable with  $E_5$  at high wave

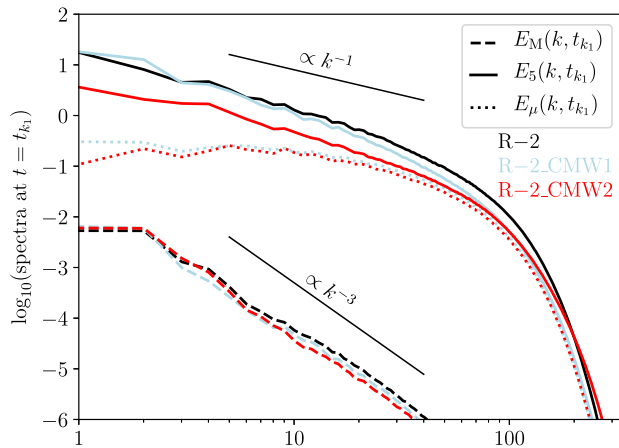


FIG. 19. Comparison of different energy spectra at time  $t = t_{k_1}$  in runs R-2, R-2CMW1, and R-2CMW2. Scaling relations of  $E_M$  and  $E_5$  seem not to be affected for the produced chiral magnetic waves. The power spectrum of the chemical potential,  $E_\mu$  which is defined in the same way as  $E_5$ , approaches  $E_5$  at high  $k$ . But  $E_\mu \ll E_5$  at small  $k$  at the time  $t_{k_1}$ .

numbers, while they are significantly lower at low wave numbers. For R-2\_CMW2, the  $E_5$  spectrum at  $t_{k_1}$  has the same scaling of  $\propto k^{-1}$  but its amplitude is almost an order of magnitude less than the ones in runs R-2 and R-2\_CMW1. This may be related to the additional shock viscosity in R-2\_CMW2.

## V. CONCLUSION

In this paper we have analyzed various dynamo instabilities that are sourced by an inhomogeneous chiral chemical potential. To this end, we performed DNS of chiral MHD with the Pencil Code. While the existence of chiral dynamo instabilities has been confirmed with DNS before, most previous studies have assumed a uniform distribution of  $\mu_5$ . In this paper we performed a detailed study of dynamo instabilities caused by an initial inhomogeneous distribution of  $\mu_5$ , which clarifies and supports the findings presented in Ref. [48], in particular the buildup of a mean  $\mu_5$  and the occurrence of a mean-field dynamo. To test the necessary conditions for a small-scale chiral dynamo, we have used a 2D toy model in which  $\mu_5$  was initialized with a sine function along one direction. Its wave number was varied to explore the effect of the effective correlation wave number  $k_{\mu_5, \text{eff}}$ . We have demonstrated that the small-scale chiral dynamo can operate if  $k_{\mu_5, \text{eff}} < k_5$ ; see Fig. 4, where  $k_5$  is the wave number based on the scale of the maximum growth rate of the small-scale chiral dynamo instability based on the maximum value of  $\mu_5$ . With larger scale separation, the measured growth rate of the rms magnetic field approaches the maximum possible value  $\gamma_5 = \eta \mu_{5, \text{max}}^2 / 4$  in the system. Saturation of the dynamo occurs once the fluctuations of the chiral chemical potential,  $\mu'_5$ , experience a backreaction from  $B_{\text{rms}}$ , leading to a change of the characteristic scale  $k_{\mu_5, \text{eff}}$ . When  $k_{\mu_5, \text{eff}}$  becomes comparable to  $k_5$ , the growth of the magnetic field stops; see Fig. 6.

Another main focus of this work was a detailed analysis of the DNS with initial fluctuations of  $\mu_5$  with zero mean described shortly in Ref. [48]. In all of our DNS that develop turbulence, i.e., which reach sufficiently large  $\text{Re}_M$ , we could confirm the presence of a mean-field dynamo; see Fig. 15. Contrary to the previously studied case of homogeneous  $\mu_5$  where the mean-field dynamo is dominated by the  $\alpha_\mu$  effect that is related to fluctuations of  $\mu_5$  itself, for inhomogeneous  $\mu_5$  the magnetic  $\alpha$  effect,  $\alpha_M$ , related to the current helicity plays the central role in the mean-field dynamo phase (see e.g., Fig. 14). The main reason for this effect is the additional source of current helicity,  $2\bar{v}_5 \bar{\mathbf{b}}^2$ , caused by magnetic fluctuations produced by inhomogeneities of  $\mu_5$ . Note that in this study we had to use the average based on the integral scale of turbulence which increases during the nonlinear evolution of the system.

Finally, we reported a tight connection between the evolution of the power spectra of magnetic energy,  $E_M(k)$ ,

and that of the chiral chemical potential,  $E_5(k)$ ; see Fig. 16. With the onset of turbulence, independently of their initial shape, both power spectra develop a power-law scaling with a negative index. Specifically, the  $E_5(k)$  spectra approach a universal scaling proportional to  $k^{-1}$ . For our reference run with homogeneous  $\mu_5$ ,  $E_M$  approaches a  $k^{-2}$  scaling, which is consistent with the results of Ref. [25]. In the runs with an inhomogeneous initial  $\mu_5$ , a slightly steeper scaling of  $k^{-3}$  develops, except for the run with an initial  $\mu_5$  in the form of a sine spatial profile (S23D), where the spectrum is closer to  $E_5 \propto k^{-2}$ .

Our results can be employed in models of primordial plasmas. Several models of the early Universe, e.g., specific scenarios of inflation or cosmological phase transitions, predict the production of primordial magnetic fields which should evolve according to the laws of chiral MHD as long as the temperature is  $> 10$  MeV. Detailed models of the evolution of the primordial magnetic fields are needed, if it is to be used to constrain fundamental physics at the time before recombination.

### ACKNOWLEDGMENTS

We have benefited from stimulating discussions with Nathan Kleorin and Abhijit B. Bendre. J. S. acknowledges the support by the Swiss National Science Foundation

under Grant No. 185863. A. B. was supported in part through a grant from the Swedish Research Council (Vetenskapsrådet, 2019-04234).

### APPENDIX A: COMPARISON BETWEEN $-\nabla^4$ AND $\nabla^2$ DIFFUSION OF $\mu_5$

In direct numerical simulations of chiral MHD, large discretization errors cause phase errors in the advection of the high wave number contributions to  $\mu_5$ . Therefore, dissipation of  $\mu_5$  on small spatial scales is required. In our previous work (e.g., Refs. [25,26]), where we considered an initially uniform  $\mu_5$ , the  $\nabla^2$  diffusion never affected the evolution of  $\mu_5$  significantly. In this study, however, we consider cases where  $\mu_5$  is concentrated at large wave numbers and therefore is affected by  $\nabla^2$  diffusion. A  $\nabla^2$  diffusion ( $-k^2$  in Fourier space) constantly reduces the value of  $\mu_5$  at moderately high  $k$  and thereby the effects of a fluctuating chiral chemical potential on the magnetic field. To prevent this loss of  $\mu_5$  before it can be converted into magnetic helicity, we have implemented a  $-\nabla^4$  diffusion ( $-k^4$  in Fourier space) that mostly acts on the highest wave numbers of the numerical domain where it is needed for numerical stability. This allows us to study the effects of a  $\mu_5$  at moderately high  $k$ .

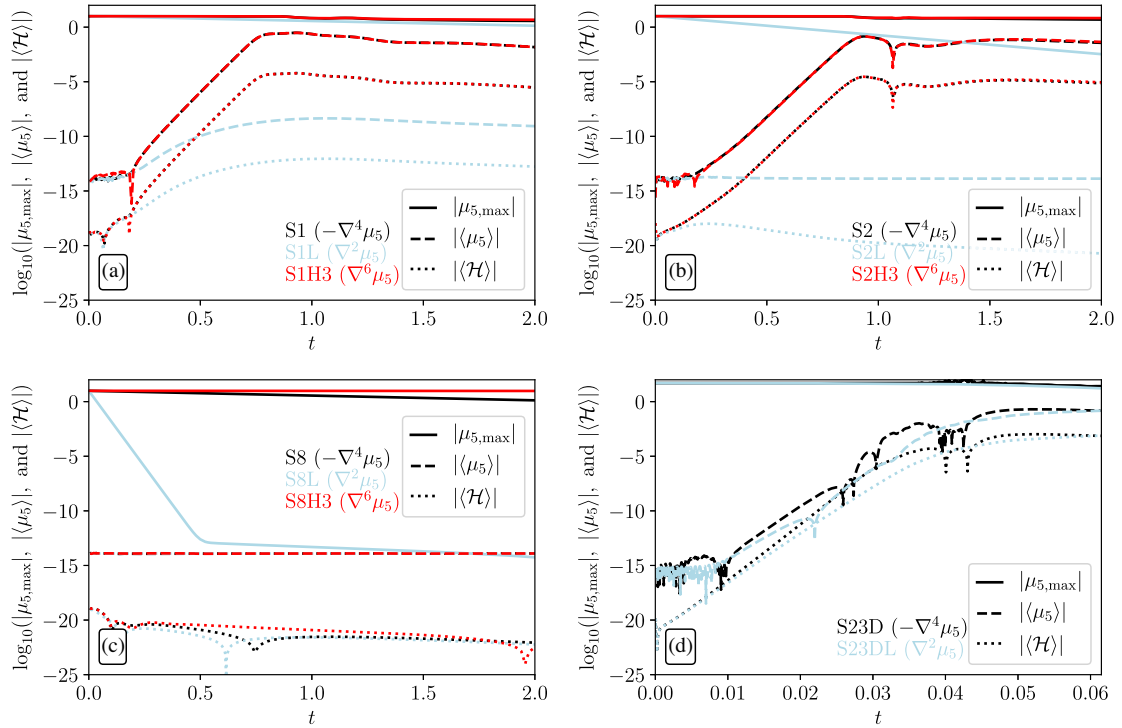


FIG. 20. Comparison between runs with the default hyperdiffusion ( $\propto -\nabla^4 \mu_5$ , black line color) and Laplacian diffusion ( $\propto \nabla^2 \mu_5$ , blue line color) and third-order hyperdiffusion ( $\propto \nabla^6 \mu_5$ , red line color). For each run, the time evolution of  $|\mu_{5,\max}|$  (solid lines),  $|\langle \mu_5 \rangle|$  (dashed lines), and  $|\langle \mathcal{H} \rangle|$  (dotted lines) is shown. (a) Runs S1, S1L, and S1H3. (b) Runs S2, S2L, and S2H3. (c) Runs S8, S8L, and S8H3. (d) Runs S23D and S23DL.

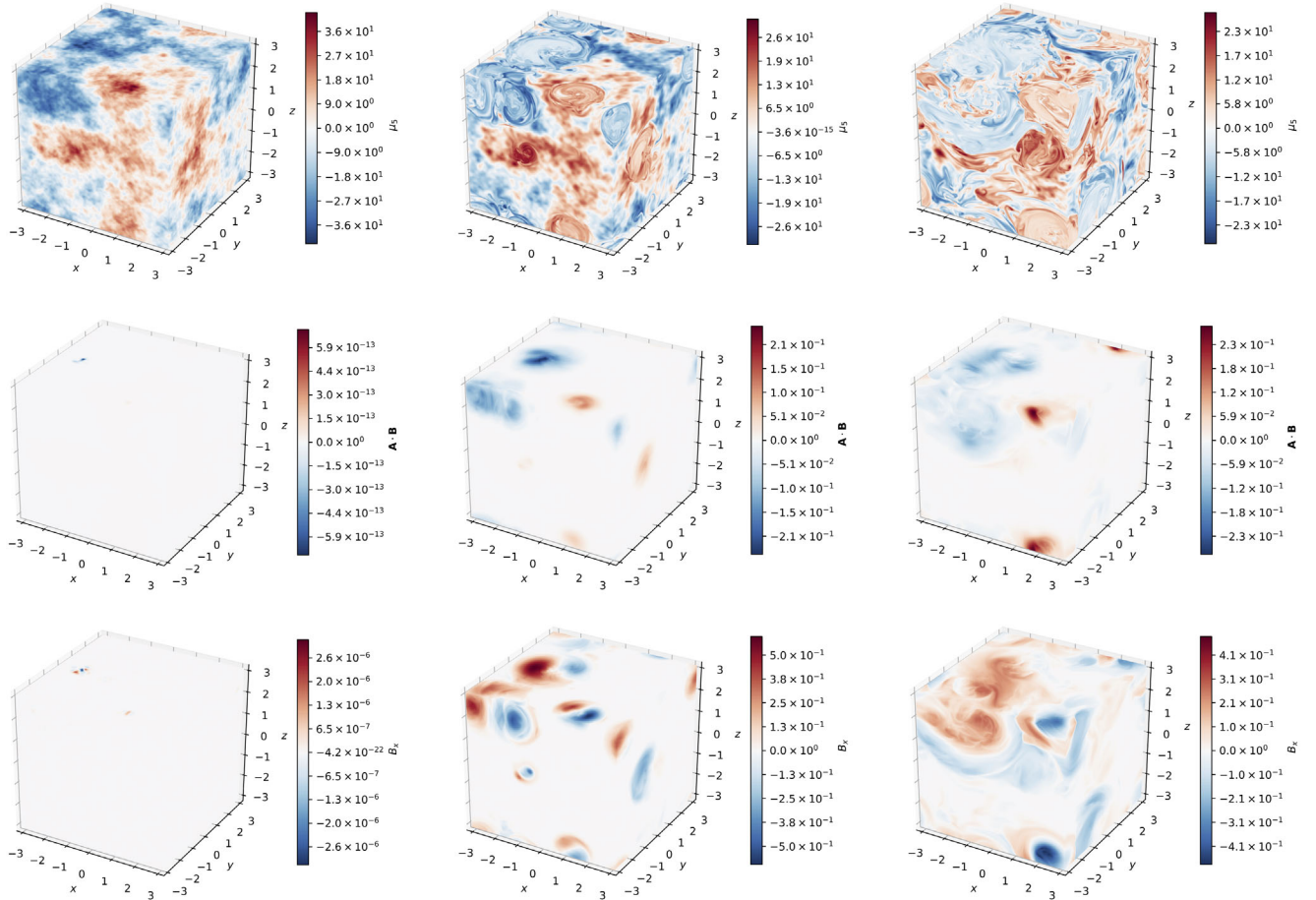


FIG. 21. Snapshots of run R – 2 taken at the different times: during the  $v_5$  dynamo phase ( $t = 0.02$ , left), the mean-field dynamo phase ( $t = 0.1$ , middle), and at the time when the inverse cascade reaches the scale of the domain ( $t = 0.135$ , right).

In Fig. 20, we present the difference between the default second-order hyperdiffusion, Laplacian diffusion, and third-order hyperdiffusion for selected runs. Runs S1, S2, S8, and S23D have been repeated with Laplacian diffusion (runs S1L, S2L, S8L, and S23DL) and we have additionally tested third-order hyperdiffusion for runs S1, S2, S8 (runs S1H3, S2H3, and S8H3). Laplacian diffusion strongly affects an inhomogeneous  $\mu_5$ , especially if its initial inverse correlation length is large in comparison to the Nyquist wave number  $k_{\text{Ny}}$ . In particular,  $|\mu_{5,\text{max}}|$  decreases faster the closer the wave number is to  $k_{\text{Ny}}$ ; compare the solid lines in Figs. 20(a)–20(c). With faster decreasing  $|\mu_{5,\text{max}}|$ , the chiral dynamo instability phase is shorter and less efficient or in extreme cases not even present when hyperdiffusion is replaced by Laplacian diffusion; see Fig. 20(b). Third-order hyperdiffusion results in very similar dynamics for the runs with an initial sine spatial profile for  $k = 1$  and  $k = 2$  (S1 vs S1H3 and S2 vs S2H3) and there is only a small difference between S8 and S8H3. For the high-resolution 3D run, S23D, the initial characteristic wave number of the dynamo instability ( $k \approx 25$ ) is much smaller than the Nyquist wave number

( $k \approx 336$ ). Therefore, the difference between second-order hyperdiffusion (run S23D) and Laplacian diffusion (S23DL) is noticeable but not very significant; see Fig. 20(d).

## APPENDIX B: SNAPSHOTS OF RUN R – 2

In Sec. IV B we discuss the time evolution of run R – 2, starting from the initial small-scale chiral instability to the amplification of the magnetic field on large scales at late times. In addition to the quantitative analysis there, we present in Fig. 21 the snapshots of run R – 2. The values of  $\mu_5$ ,  $\mathbf{A} \cdot \mathbf{B}$ , and  $B_x$  on the surfaces of the domain are shown at different times.

## APPENDIX C: TIME EVOLUTION OF POWER SPECTRA IN RUNS H2, R + 1, AND S203D

We have mentioned the mean-field chiral dynamo for the case of a uniform  $\mu_5$  in different places of the main text. For such systems the magnetic energy spectra developed a  $k^{-2}$  scaling. In Figs. 22(a) and 22(b), we

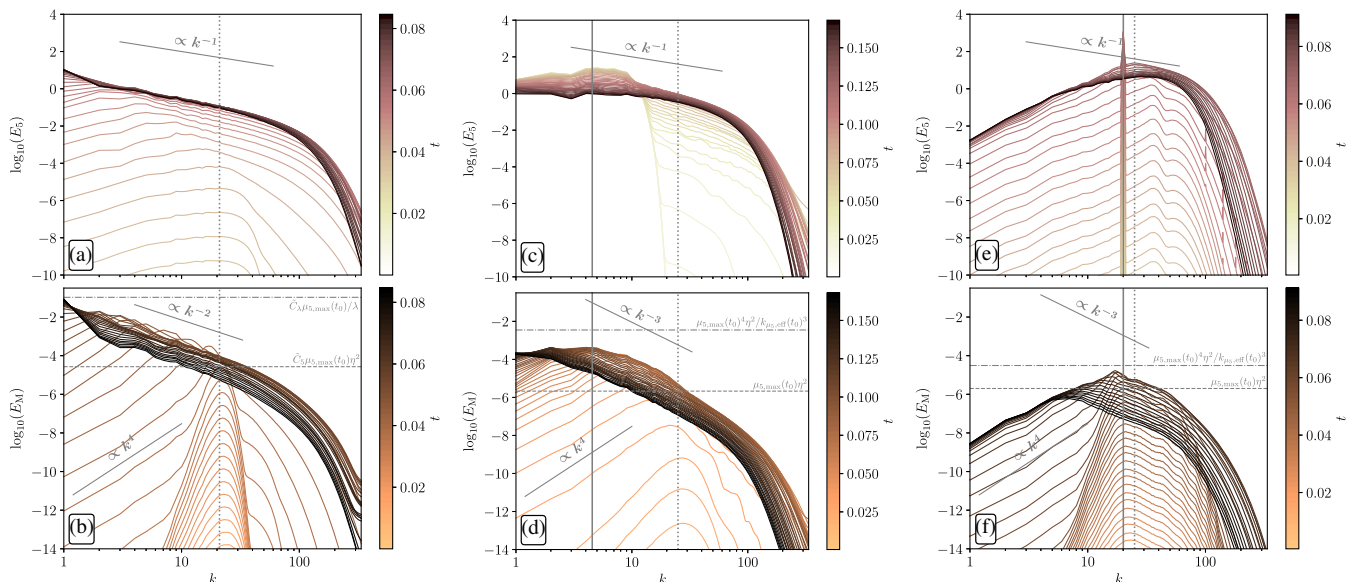


FIG. 22. Evolution of the spectra in runs H2 (with  $\tilde{C}_5 = 16$  and  $\tilde{C}_\lambda = 1$ , as reported in Ref. [25]), R + 1, and S203D.

present the energy spectra for our comparison run H2 with initially constant  $\mu_5$  and confirm the  $E_M \propto k^{-2}$  scaling, which is different from the steeper magnetic energy spectra for runs with initially inhomogeneous  $\mu_5$  and vanishing  $\langle \mu_5 \rangle$ . The  $\mu_5$  spectrum, on the other hand,

approaches a  $k^{-1}$  for all cases in which turbulence becomes sufficiently strong, hence also for H2.

We further present in Fig. 22 the spectra of run R + 1, which are referred to in Sec. IV D, and the spectra of run S203D that are mentioned in Sec. IV.

- 
- [1] H. K. Moffatt, *Magnetic Field Generation in Electrically Conducting Fluids* (Cambridge University Press, Cambridge, England, 1978).
  - [2] F. Krause and K. H. Rädler, *Mean-Field Magnetohydrodynamics and Dynamo Theory* (Pergamon, Oxford, 1980).
  - [3] Y. B. Zeldovich, A. A. Ruzmaikin, and D. D. Sokoloff, *Magnetic Fields in Astrophysics* (Gordon and Breach, New-York, 1983).
  - [4] A. Brandenburg and K. Subramanian, Astrophysical magnetic fields and nonlinear dynamo theory, *Phys. Rep.* **417**, 1 (2005).
  - [5] G. Rüdiger, R. Hollerbach, and L. L. Kitchatinov, *Magnetic Processes in Astrophysics: Theory, Simulations, Experiments* (John Wiley & Sons, Weinheim, 2013).
  - [6] A. Brandenburg, Advances in mean-field dynamo theory and applications to astrophysical turbulence, *J. Plasma Phys.* **84**, 735840404 (2018).
  - [7] I. Rogachevskii, *Introduction to Turbulent Transport of Particles, Temperature and Magnetic Fields* (Cambridge University Press, Cambridge, England, 2021).
  - [8] D. J. Stevenson, Planetary magnetic fields, *Earth Planet. Sci. Lett.* **208**, 1 (2003).
  - [9] U. R. Christensen, Dynamo scaling laws and applications to the planets, *Space Sci. Rev.* **152**, 565 (2010).
  - [10] H. K. Moffatt and E. Dormy, *Self-Exciting Fluid Dynamos* (Cambridge University Press, Cambridge, England, 2019), Vol. 59.
  - [11] E. N. Parker, *Cosmical Magnetic Fields: Their Origin and their Activity* (Clarendon Press, Oxford, 1979).
  - [12] M. Ossendrijver, The solar dynamo, *Astron. Astrophys. Rev.* **11**, 287 (2003).
  - [13] P. J. Käpylä, M. J. Korpi, and A. Brandenburg, Large-scale dynamos in turbulent convection with shear, *Astron. Astrophys.* **491**, 353 (2008).
  - [14] A. Ruzmaikin, A. M. Shukurov, and D. D. Sokoloff, *Magnetic Fields of Galaxies* (Kluwer Academic, Dordrecht, 1988).
  - [15] R. Beck, A. Brandenburg, D. Moss, A. Shukurov, and D. Sokoloff, Galactic magnetism: Recent developments and perspectives, *Annu. Rev. Astron. Astrophys.* **34**, 155 (1996).
  - [16] R. M. Kulsrud, A critical review of galactic dynamos, *Annu. Rev. Astron. Astrophys.* **37**, 37 (1999).
  - [17] J. Schober, D. R. G. Schleicher, and R. S. Klessen, Magnetic field amplification in young galaxies, *Astron. Astrophys.* **560**, A87 (2013).
  - [18] L. Chamandy and N. K. Singh, Non-linear galactic dynamos and the magnetic Rädler effect, *Mon. Not. R. Astron. Soc.* **481**, 1300 (2018).

- [19] A. Vilenkin, Equilibrium parity violating current in a magnetic field, *Phys. Rev. D* **22**, 3080 (1980).
- [20] M. Giovannini, Anomalous magnetohydrodynamics, *Phys. Rev. D* **88**, 063536 (2013).
- [21] I. Rogachevskii, O. Ruchayskiy, A. Boyarsky, J. Fröhlich, N. Kleeorin, A. Brandenburg, and J. Schober, Laminar and turbulent dynamos in chiral magnetohydrodynamics-I: Theory, *Astrophys. J.* **846**, 153 (2017).
- [22] L. Del Zanna and N. Bucciantini, Covariant and  $3+1$  equations for dynamo-chiral general relativistic magnetohydrodynamics, *Mon. Not. R. Astron. Soc.* **479**, 657 (2018).
- [23] K. Hattori, Y. Hirono, H.-U. Yee, and Y. Yin, Magnetohydrodynamics with chiral anomaly: Phases of collective excitations and instabilities, *Phys. Rev. D* **100**, 065023 (2019).
- [24] M. Joyce and M. Shaposhnikov, Primordial Magnetic Fields, Right Electrons, and the Abelian Anomaly, *Phys. Rev. Lett.* **79**, 1193 (1997).
- [25] A. Brandenburg, J. Schober, I. Rogachevskii, T. Kahniashvili, A. Boyarsky, J. Fröhlich, O. Ruchayskiy, and N. Kleeorin, The turbulent chiral-magnetic cascade in the early universe, *Astrophys. J. Lett.* **845**, L21 (2017).
- [26] J. Schober, I. Rogachevskii, A. Brandenburg, A. Boyarsky, J. Fröhlich, O. Ruchayskiy, and N. Kleeorin, Laminar and turbulent dynamos in chiral magnetohydrodynamics. II. Simulations, *Astrophys. J.* **858**, 124 (2018).
- [27] A. Boyarsky, J. Fröhlich, and O. Ruchayskiy, Self-Consistent Evolution of Magnetic Fields and Chiral Asymmetry in the Early Universe, *Phys. Rev. Lett.* **108**, 031301 (2012).
- [28] Y. Hirono, D. E. Kharzeev, and Y. Yin, Self-similar inverse cascade of magnetic helicity driven by the chiral anomaly, *Phys. Rev. D* **92**, 125031 (2015).
- [29] E. V. Gorbar, I. Rudenok, I. A. Shovkovy, and S. Vilchinskii, Anomaly-driven inverse cascade and inhomogeneities in a magnetized chiral plasma in the early universe, *Phys. Rev. D* **94**, 103528 (2016).
- [30] J. Schober, T. Fujita, and R. Durrer, Generation of chiral asymmetry via helical magnetic fields, *Phys. Rev. D* **101**, 103028 (2020).
- [31] B. A. Campbell, S. Davidson, J. Ellis, and K. A. Olive, On the baryon, lepton-flavour and right-handed electron asymmetries of the universe, *Phys. Lett. B* **297**, 118 (1992).
- [32] A. Boyarsky, V. Cheianov, O. Ruchayskiy, and O. Sobol, Evolution of the Primordial Axial Charge Across Cosmic Times, *Phys. Rev. Lett.* **126**, 021801 (2021).
- [33] D. E. Kharzeev, The chiral magnetic effect and anomaly-induced transport, *Prog. Part. Nucl. Phys.* **75**, 133 (2014).
- [34] D. E. Kharzeev, J. Liao, S. A. Voloshin, and G. Wang, Chiral magnetic and vortical effects in high-energy nuclear collisions—a status report, *Prog. Part. Nucl. Phys.* **88**, 1 (2016).
- [35] D. E. Kharzeev, L. D. McLerran, and H. J. Warringa, The effects of topological charge change in heavy ion collisions: ‘Event by event P and CP violation’, *Nucl. Phys.* **A803**, 227 (2008).
- [36] Y. Hirono, T. Hirano, and D. E. Kharzeev, The chiral magnetic effect in heavy-ion collisions from event-by-event anomalous hydrodynamics, [arXiv:1412.0311](https://arxiv.org/abs/1412.0311).
- [37] STAR Collaboration, Azimuthal Charged-Particle Correlations and Possible Local Strong Parity Violation, *Phys. Rev. Lett.* **103**, 251601 (2009).
- [38] ALICE Collaboration, Charge Separation Relative to the Reaction Plane in Pb-Pb Collisions at  $\sqrt{s_{NN}}=2.76$  TeV, *Phys. Rev. Lett.* **110**, 012301 (2013).
- [39] M. Dvornikov and V. B. Semikoz, Influence of the turbulent motion on the chiral magnetic effect in the early universe, *Phys. Rev. D* **95**, 043538 (2017).
- [40] J. Charbonneau and A. Zhitnitsky, Topological currents in neutron stars: Kicks, precession, toroidal fields, and magnetic helicity, *J. Cosmol. Astropart. Phys.* **08** (2010) 010.
- [41] A. Ohnishi and N. Yamamoto, Magnetars and the chiral plasma instabilities, [arXiv:1402.4760](https://arxiv.org/abs/1402.4760).
- [42] N. Yamamoto, Chiral transport of neutrinos in supernovae: Neutrino-induced fluid helicity and helical plasma instability, *Phys. Rev. D* **93**, 065017 (2016).
- [43] G. Sigl and N. Leite, Chiral magnetic effect in protoneutron stars and magnetic field spectral evolution, *J. Cosmol. Astropart. Phys.* **01** (2016) 025.
- [44] M. Dvornikov, V. B. Semikoz, and D. D. Sokoloff, Generation of strong magnetic fields in a nascent neutron star accounting for the chiral magnetic effect, *Phys. Rev. D* **101**, 083009 (2020).
- [45] V. Galitski, M. Kargarian, and S. Syzranov, Dynamo Effect and Turbulence in Hydrodynamic Weyl Metals, *Phys. Rev. Lett.* **121**, 176603 (2018).
- [46] J. Schober, A. Brandenburg, I. Rogachevskii, and N. Kleeorin, Energetics of turbulence generated by chiral MHD dynamos, *Geophys. Astrophys. Fluid Dyn.* **113**, 107 (2019).
- [47] J. Schober, A. Brandenburg, and I. Rogachevskii, Chiral fermion asymmetry in high-energy plasma simulations, *Geophys. Astrophys. Fluid Dyn.* **114**, 106 (2020).
- [48] J. Schober, I. Rogachevskii, and A. Brandenburg, companion Letter, Production of a Chiral Magnetic Anomaly with Emerging Turbulence and Mean-Field Dynamo Action, *Phys. Rev. Lett.* **128**, 065002 (2022).
- [49] A. Brandenburg, Y. He, T. Kahniashvili, M. Rheinhardt, and J. Schober, Relic Gravitational Waves from the Chiral Magnetic Effect, *Astrophys. J.* **911**, 110 (2021).
- [50] D. E. Kharzeev and H.-U. Yee, Chiral magnetic wave, *Phys. Rev. D* **83**, 085007 (2011).
- [51] We note that the expression (9) would be ill-defined at  $k = 0$ . Therefore integration starts at  $k = 1$  which is the minimum possible value of  $k_{\text{int}}$ .
- [52] N. Kleeorin and I. Rogachevskii, Magnetic helicity tensor for an anisotropic turbulence, *Phys. Rev. E* **59**, 6724 (1999).
- [53] A. Brandenburg *et al.* (Pencil Code Collaboration), The Pencil Code a modular MPI code for partial differential equations and particles: multipurpose and multiuser-maintained, *J. Open Source Software* **6**, 2807 (2021).
- [54] J. H. Williamson, Low-storage Runge-Kutta schemes, *J. Comput. Phys.* **35**, 48 (1980).
- [55] A. Brandenburg and W. Dobler, Hydromagnetic turbulence in computer simulations, *Comput. Phys. Commun.* **147**, 471 (2002).
- [56] A. Brandenburg, Computational aspects of astrophysical MHD and turbulence, in *Advances in Nonlinear Dynamics*,

- edited by A. Ferriz-Mas and M. Núñez (CRC Press, Bristol, 2003), pp. 269–344.
- [57] This corresponds to the scale of the  $v_5$  dynamo instability, which for S23D is  $\mu_{5,\max}(t_0)/2 = 25$ .
- [58] Indeed, even for run R – 2m which has an initial non-vanishing component of  $\langle \mu_5 \rangle$ , the average on  $k_{\text{int}}$ ,  $\langle \mu_5 \rangle_{\text{int}}$  dominates over the volume average, once turbulence sets in.
- [59] J. von Neumann and R. D. Richtmyer, A method for the numerical calculation of hydrodynamic shocks, *J. Appl. Phys.* **21**, 232 (1950).
- [60] C. Qian, C. Wang, J. Liu, A. Brandenburg, N. E. L. Haugen, and M. A. Liberman, Convergence properties of detonation simulations, *Geophys. Astrophys. Fluid Dyn.* **114**, 58 (2020).